

PAPER

Hybrid 3D model for the interaction of plasma thruster plumes with nearby objects

To cite this article: Filippo Cichocki *et al* 2017 *Plasma Sources Sci. Technol.* **26** 125008

View the [article online](#) for updates and enhancements.

Related content

- [A collisionless plasma thruster plume expansion model](#)
Mario Merino, Filippo Cichocki and Eduardo Ahedo
- [The role of instability-enhanced friction on 'anomalous' electron and ion transport in Hall-effect thrusters](#)
Trevor Lafleur and Pascal Chabert
- [Hollow cathode modeling: I. A coupled plasma thermal two-dimensional model](#)
Gaétan Sary, Laurent Garrigues and Jean-Pierre Boeuf

Hybrid 3D model for the interaction of plasma thruster plumes with nearby objects

Filippo Cichocki , Adrián Domínguez-Vázquez , Mario Merino  and Eduardo Ahedo 

Equipo de Propulsión Espacial y Plasmas (EP2), ep2.uc3m.es, Universidad Carlos III de Madrid, Leganés, Spain

E-mail: filippo.cichocki@uc3m.es

Received 8 August 2017, revised 17 October 2017

Accepted for publication 6 November 2017

Published 29 November 2017



CrossMark

Abstract

This paper presents a hybrid particle-in-cell (PIC) fluid approach to model the interaction of a plasma plume with a spacecraft and/or any nearby object. Ions and neutrals are modeled with a PIC approach, while electrons are treated as a fluid. After a first iteration of the code, the domain is split into quasineutral and non-neutral regions, based on non-neutrality criteria, such as the relative charge density and the Debye length-to-cell size ratio. At the material boundaries of the former quasineutral region, a dedicated algorithm ensures that the Bohm condition is met. In the latter non-neutral regions, the electron density and electric potential are obtained by solving the coupled electron momentum balance and Poisson equations. Boundary conditions for both the electric current and potential are finally obtained with a plasma sheath sub-code and an equivalent circuit model. The hybrid code is validated by applying it to a typical plasma plume–spacecraft interaction scenario, and the physics and capabilities of the model are finally discussed.

Keywords: plasma plumes, PIC, fluid, hybrid, EP2PLUS

1. Introduction

As the use of electric thrusters onboard modern spacecraft (S/C) continues to increase, understanding and predicting any integration issues early in the design process becomes essential. Electric thrusters, like the gridded ion thruster (GIT) or the Hall-effect thruster (HET) [1, 2], produce energetic plasma plumes that interact with the local electric and magnetic fields, and can induce electric charging, produce mechanical erosion/contamination and exert force/torque on any object they interact with [3, 4], as shown in figure 1. While minimizing this interaction on different key components, such as the solar array and onboard sensors, is crucial in modern S/C designs, plasma plumes can also be used in exotic applications like the ion beam shepherd [5–8], where a space debris object is gradually repositioned to a different orbit through the ion push of an electric thruster plume, which is directed towards it by a ‘shepherd’ S/C. The study of similar plasma jets is also relevant in other research fields, such as plasma material processing [9] and astrophysics [10, 11].

Plasma plumes from GITs and HETs are rarefied, with peak densities in the order of 10^{16} – 10^{18} m^{-3} [1, 2, 12, 13], and thus weakly collisional. In addition, they are characterized by very different dynamics for ions and electrons, with the latter being 4–5 orders of magnitude lighter, and responding much more quickly to external perturbations. As a consequence, mass and momentum are mostly due to ions, while the self-consistent electric fields depend mostly on the electrons dynamics, and are strongly affected by the presence of externally applied magnetic fields, so that analyses must distinguish between magnetized and unmagnetized plasma plumes. In general, a plasma plume features a ‘near region’ (extending up to a few thruster radii from its exit surface) and a ‘far-region’ [12, 13]. In the former, the plasma is markedly non-homogeneous, with non-negligible 3D effects due to (1) particle collisions, such as charge-exchange (CEX) collisions [14, 15] between ions and neutrals, (2) plume quasineutralization, and (3) the applied electric and magnetic fields. In the far-region, on the other hand, a smooth, more rarefied, single-peaked plume profile generally forms, and the above effects become negligible with respect to the plume kinetic

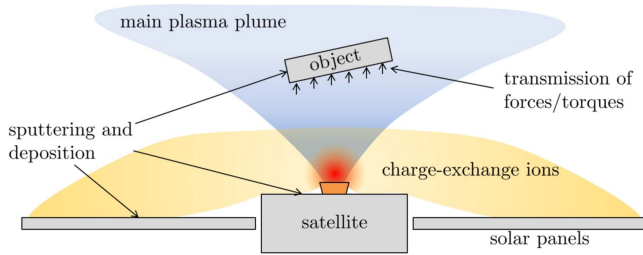


Figure 1. Schematic representation of the plasma–plume interaction with the emitting S/C and with an object immersed in it.

energy. The subsequent expansion of the plasma is here mainly governed by the residual thermal pressure, and the self-consistent ambipolar electric field. This paper focuses on unmagnetized plumes and presents a model covering both the plume near and far regions.

The above described plume physics can be modeled following different approaches, going from multi-fluid models to fully kinetic ones. Table 1 lists relevant plume models and codes. Multi-fluid models operate directly with the relevant macroscopic variables and feature at least one fluid per existing species. The main issue they present comes from the weak plasma collisionality and the consequent lack of thermodynamic equilibrium. Deviations from the Maxwellian distribution function may recommend modeling a given species as two or more fluids (distinguishing, for instance, between slow and fast ions). More importantly perhaps, fluid approaches raise uncertainties on the closure of the fluid equations and the correct expression for the pressure tensors, the heat flux vectors, and the resistive forces. The problem is usually more relevant for electrons, since often ion pressure is negligible compared to electron pressure. The simplest fluid models close electron fluid equations at the level of the momentum equation, postulating an isothermal or polytropic equation of state (e.g. a generalized Boltzmann relation). Examples are the collisionless, two-fluid models of [12, 13, 16, 17] and [18], which approximate well the plume far-region, as shown by comparison with both experiments [16, 18, 19] and more complex kinetic simulations [20]. A better suited multi-fluid model covering the near-region is that of [21], which includes collisional effects, several fluids per ion species, and a Fourier law for the heat flux of the magnetized electrons.

At the other end of the modeling approaches are the fully kinetic models [22], in which the velocity distribution functions are obtained by solving the Boltzmann equation in a 6D phase-space (position and velocity). In general, these models are totally unaffordable, except for very simplified configurations. Full particle-in-cell (PIC) models [23, 24] can be considered as a very coarse approximation to the fully kinetic models. They follow an alternative Lagrangian–Eulerian approach, in which electron and ion populations are modeled as sets of macro-particles subject to the action of electric and magnetic fields and occasional collisions. Macroscopic magnitudes are computed at the nodes of dedicated meshes extending along the physical domain. A drawback of the full-PIC models is the very small time step and cell size, as

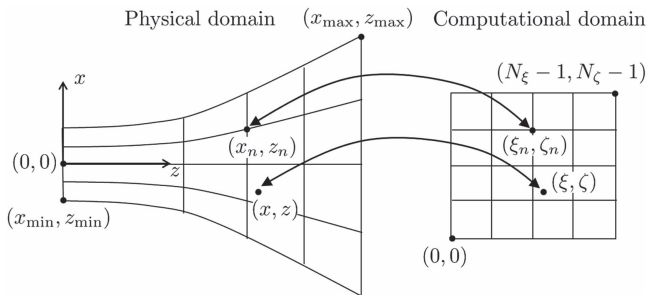
dictated by the electron small inertia and fast dynamics. Even with good parallelization, they typically require weeks or months to faithfully reproduce ion dynamics in a plasma thruster. The computational cost is even more severe for thruster plumes and their interaction with the S/C, which is an inherently 3D problem, featuring plasma density variations of several orders of magnitude, and requiring simulation domains of a few meters in all directions. Moreover, the statistical PIC noise tends to grow as the plasma expands and the number of macro-particles per cell diminishes, and this growth can be mitigated only with the use of complex population control algorithms.

An intermediate approach between full-PIC and multi-fluid models is the hybrid model [27–29, 31, 34, 35, 38–43], in which heavy particles are PIC-modeled, while electrons are treated as one or more fluids. This latter option allows us to overcome the severe constraints dictated by the electron dynamics, and to increase the computational time step by 3–4 orders of magnitude. Furthermore, while full-PIC codes are inherently non-neutral electrically and must solve the electric field from the Poisson equation, hybrid codes can assume quasineutrality in part of, or in the whole, simulation domain, thus allowing larger cell sizes and further reducing the computational time. Of course, a drawback of hybrid codes is the limited accuracy in simulating the electron dynamics (the most common fluid closure being the isothermal or polytropic electrons) but, at present, and at least for most research purposes, they constitute the best compromise in terms of accuracy, complexity and computational cost for plasma thruster and plume simulations.

This paper presents a flexible 3D hybrid PIC/fluid model and code of the interaction of a rarefied plasma plume with a S/C and/or any nearby object. A preliminary version of the code, named EP2PLUS (Extensible Parallel Plasma Plume Simulator), has already been presented in [42]. The main features are as follows. First, multiple macro-particle populations are considered in order to address not only the particle mass and charge, but also different ranges of energy, in a computationally optimal manner. Second, both direct simulation Monte Carlo (DSMC) and deterministic schemes are implemented, depending on the type of collision to be modeled. Third, population control algorithms are implemented in each cell in order to improve the macro-particles number and weight and thus reduce the statistical noise inherent in PIC formulations [44–46]. Fourth, while standard volumetric weighting is used in inner cells, more accurate surface weighting is implemented at the material boundary cells [47, 48]. Fifth, a dynamic splitting algorithm for quasineutral and non neutral regions is applied to compute the electric field in the highly inhomogeneous density regions of the domain. Sixth, Bohm condition forcing algorithms are implemented in quasineutral material boundaries in order to correctly compute the ion fluxes to the walls [47, 48]. Seventh, an equivalent electric circuit is used to deal efficiently with the different conductive walls of the S/C and the thruster, and eighth, a weakly-collisional electron fluid model is proposed, which overcomes the limitations of the typical Boltzmann relation while simultaneously yielding electron currents, and therefore

Table 1. Relevant plasma plume codes and their capabilities.

Code name or author	References	Publication date	Model type	Structured mesh	Non neutral	Electron fluid closure
Parks	[16]	1979	2D fluid	yes	no	Boltzmann
Korsun	[18, 25]	1997	2D fluid	yes	no	Boltzmann
Oh	[26]	1999	3D hybrid	yes	no	Boltzmann
Ashkenazy	[17]	2001	2D fluid	yes	no	Boltzmann
SPIS	[27–29]	2001	3D hybrid	no	yes	Boltzmann
CNES	[30]	2002	2D hybrid	yes	yes	Boltzmann
AQUILA	[31, 32]	2003	3D hybrid	no	no	polytropic
DRACO	[33]	2004	3D full-pic	yes	yes	n/a
Taccogna	[34]	2011	3D hybrid	yes	no	polytropic
USC	[23, 24]	2014	3D full-pic	yes	yes	n/a
SUGAR	[35, 36]	2014	3D hybrid	no	no	Boltzmann
EASYPLUME	[12, 13]	2015	2D fluid	yes	no	polytropic
Greifswald university	[37] [38]	2014 2015	3D full-pic 2D hybrid	yes yes	yes yes	n/a polytropic
Hall2De	[21]	2015	2D fluid	yes	no	heat flux
New Mexico State university	[39]	2015	3D hybrid	yes	no	heat flux
SM/MURF	[40]	2016	3D hybrid	no ¹	yes	polytropic

¹ Both structured and unstructured meshes can be used.

Figure 2. (a) Physical and computational domains associated with the PIC mesh. For the sake of clarity, a 2D x, z plane slice of the domain is shown.

allowing the simulation of the current neutralization at the thruster exit. Finally, the presented model is validated by applying it to a typical S/C–plume interaction scenario, and its physics and capabilities are discussed.

Regarding the paper structure, section 2 presents the features of the PIC model, while section 3 describes the electron fluid model. The quasineutral fluid closure is presented in section 4, while the approach followed for solving non-neutral plasma regions is reported in section 5. Section 6 summarizes the model, and, finally, section 7 presents and discusses the results of the S/C–plume interaction.

2. The PIC model for heavy species

In the PIC model, the distribution functions of the heavy species are discretized in both position and velocity, following a Lagrangian approach with Dirac delta functions [49]:

$$F(\mathbf{r}, \mathbf{v}, t) \approx \sum_{p=1}^N \delta(\mathbf{r} - \mathbf{r}_p(t)) \delta(\mathbf{v} - \mathbf{v}_p(t)), \quad (1)$$

where \mathbf{r}_p and \mathbf{v}_p are the position and velocity vectors of the p^{th} macro-particle. In order to reduce the computational cost of the simulation, at the cost of a higher statistical noise, a limited number N of macro-particles is used, each of them representing a very large number W of elementary particles, referred to as the macro-particle weight. The motion of each macro-particle in the electromagnetic field is solved by integrating the corresponding Newton equation, while its collisions with other macro-particles and with the material surfaces of the domain are simulated as instantaneous events (the real interaction time is indeed much shorter than the integration time step). The distribution functions are then weighted to the nodes of a dedicated PIC mesh in order to obtain Eulerian weighted properties at specific positions, used by the fluid closure model to obtain self-consistent fields. This hybrid Lagrangian–Eulerian approach allows us to reduce the number of elementary operations to be carried out at every time step to $O(N)$, versus the $O(N^2)$ number of operations of molecular dynamics codes [49].

2.1. General features

As shown in table 1, hybrid codes can make use of either unstructured or structured meshes. In this work, a structured mesh is used, given its higher computational efficiency in terms of macro-particle sorting algorithms, at the cost of a lower flexibility when dealing with complex object geometries. In a structured mesh, each position vector is identified by a set of three computational coordinates (ξ, η, ζ) , which have a bijective relation with the corresponding physical coordinates (x, y, z) , as shown in figure 2. If N_ξ, N_η, N_ζ are the numbers of nodes along the three coordinate directions, then the computational coordinates vary respectively in the ranges $[0, N_\xi - 1]$, $[0, N_\eta - 1]$ and $[0, N_\zeta - 1]$. A typical cell features a side of approximately 1 cm, whereas the Debye length varies from fractions of mm, to tens of cm. Regarding the number of nodes, this is around 10^6 , i.e. the simulation

domain typically features 100 nodes along each coordinate direction.

In order to maintain the stability of the integration scheme, the PIC time step Δt is selected so that the fastest macro-particles do not cross more than one cell per time step [50]. The particle mover is based on Boris' CYLRAD algorithm [51], a generalization of the second order leap frog integration, and hence with the velocity and position of the macro-particles referring to interleaved time points (separated by $\Delta t/2$). In the following, k represents the current PIC time step, so that macro-particle positions are known at time k , while velocities are known at time $k - 1/2$.

Macro-particles are grouped into L different populations, each of them stored in a dedicated computational list in terms of their atomic mass m , their charge number Z , and their origin or characteristic kinetic energy. The division of macro-particles of the same type and charge in terms of this last property is used to achieve better statistics and can also enable the use of different Δt for fast and slow particles as a means to accelerate the simulation. The clearest example is that of the CEX collision, in which the 'slow ions' and 'fast neutrals' produced by this event are stored in dedicated populations, independent of the 'fast ions' and 'slow neutrals'.

Once the macro-particles of each population have been moved, they are assigned or sorted to the corresponding cells. In a structured mesh, the corresponding cell indices are efficiently obtained as the integer part of the macro-particle computational coordinates. A first order cloud-in-cell shape [52] is then considered to weight the macro-particle to each mesh node. The particle density of a generic population is then obtained as:

$$n = \frac{1}{\Delta V} \sum_{p=1}^N W_p (1 - |\xi'_p|)(1 - |\eta'_p|)(1 - |\zeta'_p|), \quad (2)$$

where ΔV is the volume associated with the PIC mesh node (which, for inner nodes of a Cartesian mesh, coincides with the physical cell volume), N is the number of macro-particles of the considered population belonging to adjacent cells, and $(\xi'_p, \eta'_p, \zeta'_p)$ are the computational coordinates of the p^{th} macro-particle, relative to the considered node.

2.2. Macro-particle collisions

Although the plasma plume is only weakly collisional, it is still affected by a large variety of collisional processes, especially in the near-region. For our intended applications the most relevant ones are:

- Ionization collisions: $A + e \rightarrow A^+ + 2e$, $A + e \rightarrow A^{++} + 3e$, and $A^+ + e \rightarrow A^{++} + 2e$.
- Symmetric and pure CEX collisions: $A^+(\text{fast}) + A(\text{slow}) \rightarrow A^+(\text{slow}) + A(\text{fast})$ and $A^{++}(\text{fast}) + A(\text{slow}) \rightarrow A^{++}(\text{slow}) + A(\text{fast})$.

Regarding the former, higher ionization degrees are irrelevant in most plasma plumes, given their increasing ionization energies and hence decreasing reaction rates. Regarding the CEX collisions, the ones considered are the resonant-symmetric reactions, with no momentum exchange.

Such reactions are the dominant collisions in a plasma plume and have the highest cross sections, as shown in [13–15] and [53]. The assumption of a zero momentum exchange is a good approximation for resonant CEX, also accepted in more complex ion–neutral collision models, like that of [53], in which the collision outcome is either a pure CEX or an elastic momentum exchange collision (MEX).

MEX collisions have generally little importance in a plasma plume. Ion–ion MEX collisions, due to Coulomb interaction, modify the affected particle relative velocity (for an ion species emitted by a plasma thruster, this amounts to fractions of eV in terms of energy), which is much smaller than their absolute velocity (thousands of eV), so that their effect is clearly negligible. MEX collisions between ions and neutrals, or between ions of different charge, on the other hand, can produce larger effects. However, their importance with respect to that of the CEX is still small, as shown in [54] and [55], especially when it comes to determining the backscattering ion flux towards the satellite, almost entirely constituted by slow CEX ions.

Although excitation collisions are an important factor of energy loss inside a plasma thruster, their effect in the dynamics of a plasma plume is also negligible. From a PIC point of view, these collisions create a macro-particle belonging to a different excited population, with possibly different collision cross sections, but with the same charge number Z . This is clearly a second order effect, since only the collision properties (but not the trajectory) of those few macro-particles that suffer an excitation collision are affected. Finally, recombination collisions are also neglected, given their low frequency in a cold rarefied plasma plume.

In the following, the cell-wise algorithms for the considered collisions are presented.

2.2.1. Ionization collisions. The approach considered here is similar to that of HP-HALL [44], and takes into account the different weights of the neutral and ion populations. In order to describe the general approach, we illustrate the particular case of $A + e \rightarrow A^+ + 2e$. First, all neutral macro-particles (i.e. the input population) are sampled to have their weight reduced due to ionization (deterministic sampling). Then, the ionization rate $R_{01}(T_e)$ is evaluated at the cell center with the Drawin model [56], with the knowledge of the electron temperature T_e (the Drawin model and the Bell model [57] are used respectively for the other reactions $A + e \rightarrow A^{++} + 3e$ and $A^+ + e \rightarrow A^{++} + 2e$).

The mass of new singly-charged ions, Δm_i , to be generated in the cell of physical volume V_c during time Δt is

$$\Delta m_i = n_e n_n m R_{01}(T_e) V_c \Delta t, \quad (3)$$

where n_e and n_n are the electron and neutral densities at the cell center. Then, the average number of new ion macro-particles is $\Delta N = \Delta m_i / (m W_{\text{gen}})$, rounded appropriately, where W_{gen} is the generation weight associated with both the cell and the output ion population (refer to section 2.5). The position of the new ion macro-particles is uniformly distributed within the cell, and their velocity is sampled from a Maxwellian distribution, with the mean velocity and temperature equal to those of the neutrals. Finally, the

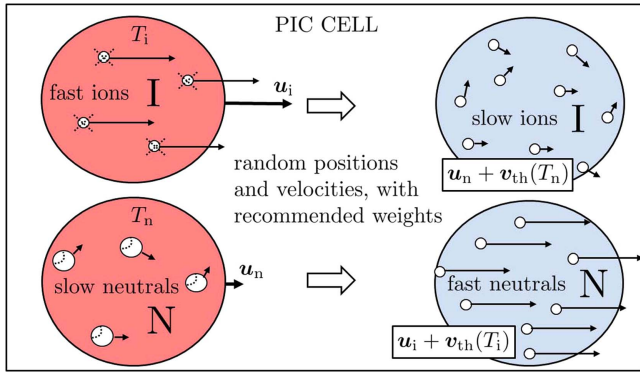


Figure 3. CEX DSMC sampling (left) and generation (right). The sampled ion macro-particles are removed from the simulation, and the weights of the sampled neutrals are reduced by the corresponding amount.

weights of all the neutral macro-particles in the cell are updated by reducing them proportionally to their values, with a total reduction in the cell of $-\Delta m_i/m$.

2.2.2. CEX collisions. Given the two input populations (e.g. fast ions and slow neutrals), the first step is to sample the macro-particles that undergo a CEX collision. A DSMC approach has been implemented; existing macro-particle pairs are checked for collision (each pair constituted by one ion and one neutral macro-particle), and a specific pair collides if a random number U is lower than its collision probability $p_{c,pair}$:

$$p_{c,pair} = \frac{1 - \exp(-\sigma(v_r)n_n v_r \Delta t)}{N_n}, \quad (4)$$

where σ is the collision cross section, v_r the relative velocity between the macro-particles of the pair, n_n the elementary number density of the neutral population, N_n the number of neutral macro-particles inside the cell, and Δt must not be larger than the expected collision time. Given the high number of pairs to be checked ($N_i N_n$), a more efficient DSMC version [49] has been adopted that limits this number to $p_{c,max} N_i N_n$, with $p_{c,max} = p_{c,pair}(|v_r \sigma(v_r)|_{max})$ representing the maximum expected collision probability for the pair. The random number U is then compared to the ratio $p_{c,pair}/p_{c,max}$, thus resulting in a more efficient macro-particle sampling (e.g. less probability checks, with a higher collision acceptance probability).

The functional dependence of the CEX cross section $\sigma(v_r)$ can be found in appendix A.1. After the sampling step, new macro-particles have to be generated in the slow ion and fast neutral populations. Referring to figure 3, these are uniformly distributed within the cell and have the generation weight of the corresponding cell and output population.

Regarding their velocities, these are sampled from a local Maxwellian distribution with the mean velocity and temperature given by the corresponding input population. This means that the slow ions feature a fluid velocity and temperature equal to that of the slow neutrals, while the fast neutrals have the same fluid properties of the fast ions.

Finally, the input populations are updated pair by pair, meaning that the weight of the heavier macro-particle is

Table 2. Existing surface types. Macro-particles are injected according to given injection profiles from the injection cells.

Element type	Effect on ions	Effect on neutrals
Transparent	none	none
Particle sink	removal	removal
Injection	stochastic injection	stochastic injection
Material wall	recombination	reflection

updated by subtracting the weight of the lighter macro-particle, which is removed from the simulation. An acceptance–rejection scheme prevents the algorithm from producing very small residual macro-particles when the input weights are very similar, while preserving mass on average.

2.3. The surface interaction and particle injection

Macro-particles can interact with boundary faces in boundary cells, representing material, injection or sink surfaces. The use of a structured mesh allows us to identify any cell-face with a set of three indices, which are used to fill a 3D matrix containing the corresponding surface types, each one identified by a specific integer value. Table 2 summarizes the surface types considered here.

By monitoring the variations of the integer part of the macro-particle computational coordinates, a crossing-detection algorithm verifies if it has crossed a boundary face. If this happens, the macro-particle is sorted for surface interaction, consisting of applying the effect of surface interaction on it, and adding its contribution to surface-weighting in that face.

2.3.1. Effects on macro-particles. The effects depend on the surface type. First, if the macro-particle crosses a sink boundary-face, such as a vacuum boundary, the macro-particle is simply removed from the domain.

Second, at injection boundary faces, like the exit surface of a plasma thruster, macro-particles are stochastically generated with the algorithms of [49]. These consider an injected particle flux g_{inj} and a probability distribution function for injection

$$f_{inj}(\mathbf{v}) \propto v_{\perp} \exp\left(-\frac{m|\mathbf{v} - \mathbf{u}_{inj}|^2}{2T_{inj}}\right), \quad (5)$$

where \mathbf{u}_{inj} and T_{inj} are the injection fluid velocity and temperature, and v_{\perp} is the cell-face perpendicular component of the macro-particle velocity. The injected macro-particle position is uniformly distributed across the injection face, and the number of injected particles depends on g_{inj} and on the generation weight W_{gen} of the injection cell. In order to simulate a continuous injection, each injected macro-particle is advanced, along its velocity direction, a random fraction of the PIC time step. With regards to macro-particles (ions or neutrals) crossing an injection face from within the plasma, they are simply re-injected as additional neutrals by the above described algorithm.

When crossing a material boundary face, ion macro-particles recombine into neutrals, while neutral macro-particles suffer either a specular or a diffuse reflection with

a defined probability. While the neutral specular reflection is simply simulated by inverting the normal velocity component of the macro-particle, the neutral re-injection due to both ion recombination or neutral diffuse reflection is carried out independently for each impacting population. The mean re-injection energy is

$$\bar{E}_{\text{reinj}} = \alpha_W 2T_W + (1 - \alpha_W) \bar{E}_{\text{imp}}, \quad (6)$$

where T_W is the wall temperature (in energy units), α_W is a wall accommodation coefficient, and \bar{E}_{imp} is the time-averaged wall-impact kinetic energy (per elementary particle) for the impacting population.

Regarding the angular distribution of the emission, a thermal cosine emission law is assumed for the injection probability distribution function, which is equivalent to using equation (5), with $\mathbf{u}_{\text{inj}} = \mathbf{0}$, and $2T_{\text{inj}} = \bar{E}_{\text{reinj}}$. Just like the injection and collisions, the re-injected neutral macro-particles feature the generation weight W_{gen} of the corresponding cell.

For those material interfaces immersed in a quasineutral region (see section 5), the sheath potential fall must be taken into account in order to determine \bar{E}_{imp} (equation (6)) and the energy flux to the wall of ion macro-particles. If ϕ_S is the sheath edge potential, ϕ_W is the wall potential, and $E_{\perp S}$ and $E_{\parallel S}$ the kinetic energies (per elementary particle) normal and parallel to the sheath edge, ion macro-particles reach the wall if

$$E_{\perp W} = E_{\perp S} + eZ(\phi_S - \phi_W) > 0,$$

and with an impact energy (per elementary particle) $E_{\text{imp}} = E_{\perp W} + E_{\parallel S}$. Otherwise they are treated as specularly reflected from the sheath edge.

2.3.2. Surface-weighting. Extended surface weighting algorithms were introduced in [48] and [47] and provide more accurate results for macroscopic variables than volumetric weighting at boundary faces and nodes. Simple surface weighted density and particle flux vectors are defined as:

$$n_{\text{sw}} = \frac{1}{\Delta t \Delta S} \sum_{p=1}^{N_{\text{hit}}} \frac{W_p}{|v_{\perp,p}|}, \quad (7)$$

$$\mathbf{g}_{\text{sw}} = (n\mathbf{u})_{\text{sw}} = \frac{1}{\Delta t \Delta S} \sum_{p=1}^{N_{\text{hit}}} \frac{W_p \mathbf{v}_p}{|v_{\perp,p}|}, \quad (8)$$

where $v_{\perp,p}$ is the p^{th} macro-particle perpendicular velocity (with respect to the cell-face), N_{hit} is the number of hitting (from the plasma) or emitted (towards the plasma) macro-particles in the current time step, and ΔS is the boundary face area. Since few particles typically cross a boundary face in a single time step, the extended time-averaged version

$$\bar{n}_{\text{sw}}^{(k)} = \frac{(\Delta k_{\text{avg}} - 1) \bar{n}_{\text{sw}}^{(k-1)} + n_{\text{sw}}}{\Delta k_{\text{avg}}} \quad (9)$$

is used for the density, and similarly for other variables, with Δk_{avg} the averaging number of time steps, and k and $k - 1$ meaning two consecutive time steps. These time-averaged

surface-weighted ion and plasma properties are finally interpolated from cell-faces to mesh nodes at the material boundaries.

2.4. The Bohm condition forcing

In most or all quasineutral material boundary faces (refer to section 5) there is a ‘negative’ sheath with $\phi_W < \phi_S$, thus attracting ions. For a collisionless and unmagnetized sheath, a stable solution exists if ions fulfill the kinetic Bohm condition [47, 48, 58], at the sheath edge

$$\sum_{s=1}^L \int_0^{\infty} \left(\frac{Z_s}{T_e} - \frac{Z_s^2}{m_s v_{\perp}^2} \right) F_s(v_{\perp}) dv_{\perp} \geq 0, \quad (10)$$

where L is the total number of particle populations and F_s is the distribution function of the s^{th} population at the sheath edge (integrated over parallel velocities). The surface-weighted PIC version of the Bohm condition is

$$P \equiv \frac{1}{\Delta t \Delta S} \sum_{s=1}^L \sum_{p=1}^{N_{\text{hit}}} \frac{W_p}{|v_{\perp,p}|} \left(\frac{Z_s}{T_e} - \frac{Z_s^2}{m_s v_{\perp,p}^2} \right) \geq 0, \quad (11)$$

where m_s is the elementary mass of the s^{th} population. Observe that the evaluation of P with this surface weighting scheme allows us to avoid the singularity existing for $v_{\perp,p} = 0$, since all macro-particles crossing the boundary faces necessarily have a non-zero normal velocity.

It is also well known that the electric field perpendicular to the wall changes quickly near the sheath edge. Ahedo and Parra [47] showed that the Bohm condition was far from being satisfied for typical cell sizes in a quasineutral PIC code and proposed the Bohm condition forcing algorithm [47, 48] as the most efficient way to fulfill equation (10). The algorithm can be understood as a virtual transition layer between the boundary simulation domain and the sheath (much thinner than the cell size and much thicker than the Debye length) that adapts the electric potential to satisfy the Bohm condition by acting on n_e . Whenever $P < 0$ in equation (11), the algorithm introduces a potential fall $\delta\phi$, which increases the perpendicular velocity $v_{\perp,p}$ in order to have $P \simeq 0$. Ahedo et al [47] showed that the correction delta-phi required to satisfy the Bohm condition decreases over time.

2.5. The PIC population control

In PIC codes, controlling the macro-particle number and weight is fundamental for low statistical noise, accurate collision algorithms and optimal computational cost. The goals of population control algorithms are therefore to (1) ensure that the number of macro-particles per cell is within a desired interval $[N_{\text{min}}, N_{\text{max}}]$, and (2) to minimize the weight dispersion within each cell. Possible actions to achieving them are:

- Use of a non-uniform physical mesh adapted to the local species density. Larger cells improve the velocity-space resolution at the cost of a lower physical-space resolution.

- Active control of generated macro-particle number or weight in collision and surface interaction algorithms. This approach is conditional upon the existence of sufficient collisional and surface interaction events in or near the PIC cells where the population must be controlled.
- Use of a weight re-normalization algorithm, which either splits or groups existing macro-particles, while conserving both their overall momentum and energy [59, 60].

At present, the first two solutions have been implemented. An example of the first one was illustrated in [42] where a conical mesh dramatically reduced the numerical noise downstream of a plasma plume. The second approach is described here.

Sections 2.2 and 2.3 already mentioned the use of a generation weight $W_{\text{gen}} = W_{\text{gen}}(\mathbf{r})$, for each cell and particle population. A dedicated algorithm updates such a generation weight in all cells by monitoring the current number of macro-particles per cell N_c , and the average weight of the existing macro-particles \bar{W} in the cell. Let N_{ig} be a targeted number of macro-particles per cell within the interval $[N_{\text{min}}, N_{\text{max}}]$. Then, if at least one macro-particle has been generated or injected in the considered cell in the latest time step, the generation weight is simply updated as $W_{\text{gen}} = \bar{W}N_c/N_{\text{ig}}$. Thus the generation weight represents the target value that a renormalization algorithm should consider, in splitting or merging macro-particles, in order to achieve the targeted number of macro-particles per cell. The use of an average number of macro-particles in the cell allows us to reduce the oscillations in the generation weight, thus resulting in a more reliable and robust algorithm.

3. The electron fluid model

The fluid model for electrons, complemented with the Poisson equation for the electric potential ϕ , allows us to compute their density n_e , temperature T_e , and current density $\mathbf{j}_e = -en_e\mathbf{u}_e$. As pointed out in section 1, since electrons are weakly-collisional, local thermodynamic equilibrium cannot be invoked and the closure of the fluid equations is delicate. If collisions are introduced through standard resistive terms, the main concern is in the expressions of the pressure tensor \mathcal{P}_e (in the momentum equation) and of the heat flux (in the energy equation), in the collisionless limit. Both should be derived from a kinetic approach, and several attempts are under progress in this regard, both for magnetized and unmagnetized plumes [23, 61–63, 71] and even for anisotropic plasmas [64], showing a combination of near-isothermal and polytropic behaviors.

A key point is that, if an auxiliary kinetic model is used (and collisionality is weak), a closure of the fluid equations at the level of the momentum equation is the most convenient. Thus, the proposed electron fluid model consists of the following equations:

$$\frac{\partial \rho_e}{\partial t} + \nabla \cdot \mathbf{j} = 0, \quad (12)$$

$$0 = -\nabla \cdot \mathcal{P}_e - en_e(-\nabla\phi + \mathbf{u}_e \times \mathbf{B}) - \sum_{s=1}^L \nu_{es} m_e n_e (\mathbf{u}_e - \mathbf{u}_s), \quad (13)$$

$$\nabla^2 \phi = -\frac{\rho_e}{\epsilon_0}, \quad (14)$$

where the charge and electric current densities satisfy

$$\rho_e = e(n_e^* - n_e), \quad n_e^* = \sum_{s=1}^L Z_s n_s, \quad (15)$$

$$\mathbf{j} = \mathbf{j}_i + \mathbf{j}_e, \quad \mathbf{j}_i = e \sum_{s=1}^L Z_s n_s \mathbf{u}_s, \quad \mathbf{j}_e = -en_e \mathbf{u}_e. \quad (16)$$

In addition, n_s and \mathbf{u}_s are the fluid velocity of the s^{th} heavy species population, obtained from the PIC model, \mathbf{u}_e is the electron fluid velocity, n_e^* is the quasineutral electron density, and ν_{es} is the electron momentum transfer collision frequency with population s (refer to appendix A.2 for more details).

For the purposes of the present paper, we will limit the electron fluid model to an unmagnetized plume ($\mathbf{B} = 0$) and to the simple polytropic electron closure:

$$\mathcal{P}_e = p_e \mathcal{I} \quad \text{with} \quad p_e(n_e) = n_e T_e, \quad T_e = T_{e0} \left(\frac{n_e}{n_{e0}} \right)^{\gamma-1}, \quad (17)$$

where γ is the constant polytropic coefficient, and n_{e0}, T_{e0} are the electron density and temperature at the plume location where we have set $\phi = 0$. Such a polytropic cooling approximation allows us to reproduce the major features of a plume expansion in terms of plasma density, as demonstrated by experiments [19, 65–70], fully kinetic simulations [71], and comparisons between polytropic fluid and full-PIC models [72].

Thus, equation (13) becomes

$$0 = -\nabla p_e + en_e \nabla \phi + \frac{m_e \nu_e}{e} (\mathbf{j} - \mathbf{j}_d), \quad (18)$$

where

$$\nu_e = \sum_{s=1}^L \nu_{es}, \quad \mathbf{j}_d = \mathbf{j}_i - \frac{en_e}{\nu_e} \sum_{s=1}^L \nu_{es} \mathbf{u}_s \quad (19)$$

are the total electron collision frequency and a driving current density (it shall appear as a forcing term in the final differential equation), respectively. Solving the momentum equation for \mathbf{j} , the generalized Ohm law is finally obtained:

$$\mathbf{j} = \frac{\sigma_e}{e} \nabla H_e + \mathbf{j}_d, \quad (20)$$

where $\sigma_e = e^2 n_e / \nu_e m_e$ is the electron conductivity,

$$H_e = h_e - e\phi \quad (21)$$

is the electron Bernoulli function, and

$$h_e(n_e) = \begin{cases} T_{e0} \ln \left(\frac{n_e}{n_{e0}} \right), & \gamma = 1 \\ -\frac{\gamma T_{e0}}{(\gamma-1)} \left[1 - \left(\frac{n_e}{n_{e0}} \right)^{\gamma-1} \right], & \gamma > 1 \end{cases} \quad (22)$$

is the barotropic function, satisfying $\nabla h_e = \nabla p_e / n_e$. Notice that we have set $h_e, H_e = 0$ at the location where $\phi = 0$.

Introducing equation (20) into equation (12), an elliptic differential equation for H_e is obtained:

$$\nabla^2 H_e + \nabla \ln \sigma_e \cdot \nabla H_e = -\frac{e}{\sigma_e} \left(\nabla \cdot \mathbf{j}_d + \frac{\partial \rho_c}{\partial t} \right). \quad (23)$$

Therefore, the fluid model reduces basically to solving two coupled elliptic equations: the above one for H_e and the Poisson equation for ϕ . Typical boundary conditions set either these magnitudes or the derivatives perpendicular to the walls. In the case of the Bernoulli function, the perpendicular derivative is indeed a condition on the electric current density:

$$\frac{\partial H_e}{\partial \mathbf{1}_\perp} = \frac{e}{\sigma_e} (\mathbf{j} - \mathbf{j}_d) \cdot \mathbf{1}_\perp,$$

where $\mathbf{1}_\perp$ is the unit vector normal to a considered boundary and directed towards the plasma.

4. The quasineutral closure

Let us consider first the zero Debye length limit, for which the whole plume can be considered quasineutral. The mathematical structure of the electron problem simplifies. First of all, the Poisson equation reduces to

$$n_e = n_e^* \quad (\text{i.e. } \rho_c = 0), \quad (24)$$

which determines the electron density and, subsequently, the electron temperature $T_e^* = T_e(n_e^*)$, the barotropic function $h_e^* = h_e(n_e^*)$, the conductivity $\sigma_e^* = \sigma_e(n_e^*)$, and the driving current $\mathbf{j}_d^* = \mathbf{j}_d(n_e^*)$. Notice that all these quantities are functions of the PIC model solution. The uncoupled equation for the Bernoulli function then simplifies to:

$$\nabla^2 H_e + \nabla \ln \sigma_e^* \cdot \nabla H_e = -\frac{e}{\sigma_e^*} \nabla \cdot \mathbf{j}_d^*. \quad (25)$$

Once the solution for H_e is obtained, \mathbf{j} is given by the generalized Ohm equation, equation (20), and the electric potential from equation (21), that is:

$$\phi = \frac{h_e - H_e}{e}. \quad (26)$$

Notice that the widely-used isothermal and polytropic models, leading to Boltzmann-like relations, correspond to setting $H_e \equiv 0$ in equation (26), which is the solution in the collisionless limit $\sigma_e^* \rightarrow \infty$ of equation (25). Furthermore, in this limit, the electric current in the generalized Ohm law, equation (20), is indefinite, which is the most severe limitation of the Boltzmann relation/polytropic models. The present weakly-collisional model overcomes that limitation by computing the contribution of $\sigma_e \nabla H_e / e$ to the net electric current. The simulations of section 7 will show that this contribution is central to studying the plasma plume neutralization (at the exit of GITs or HETs, for instance), and the plume-S/C interaction.

4.1. The sheath model

In the quasineutral closure, infinitely-thin Debye sheaths are postulated between the quasineutral solution and the walls in order to accommodate potentials and electric currents there. Thus, at such boundaries, we must distinguish between the wall potential ϕ_w , and the potential at the sheath edge ϕ_s (of the quasineutral solution). The sheath model then establishes a relation between these two potentials and the perpendicular current density to the wall $j_w = \mathbf{j} \cdot \mathbf{1}_\perp = j_{i,w} + j_{e,w}$ (positive if emitted by the wall, for $\mathbf{1}_\perp$ oriented towards the plasma).

In the most common case of a ‘negative’ sheath, it is $\phi_w < \phi_s$, in order to confine electrons. The well-known solution for a negative planar (and collisionless) sheath, assuming a Maxwellian-like electron distribution at its edge, relates ϕ_w and j_w through:

$$\phi_w = \phi_s - \frac{T_e}{e} \ln \left(\frac{(j_w - j_{i,w}) \sqrt{2\pi m_e}}{en_e T_e} \right), \quad (27)$$

where the ion current density, the electron density n_e and temperature T_e refer to the sheath edge.

In the case of a dielectric wall, the net-current free condition $j_w = 0$ yields ϕ_w locally. This is also the case for current-emitting walls (by thermoemission, photoemission, thermionic emission) where j_w is known locally from the PIC model solution (or from known wall heating/illumination conditions). Note that the approach considered by some full-PIC models of accumulating a local surface charge density [72, 73] has not been considered here. In fact, while enabling the simulation of the short wall charging transient, such an approach would need an implicit solver, because, in this hybrid code context, the electron current to the wall depends explicitly on the unknown wall potential.

For conductive walls (being emissive or not), the problem is more complex, since the boundary condition is non-local. Typically, from the knowledge of the electric potential ϕ_w , we compute the total electric current to a conductive wall (or object) as

$$I_w = -\sum j_w \Delta S, \quad (28)$$

where the summation extends over the material boundary faces of the conductive object, and j_w satisfies equation (27).

Furthermore, conductive walls can present locally positive sheaths, i.e. locations with $\phi_w > \phi_s$. In these locations, the current density is approximated by

$$j_w \simeq j_{i,w} - en_e \sqrt{T_e / (2\pi m_e)}.$$

For a positive planar sheath, the electron current thus equals the thermal flux in the plasma, and the PIC model must take into account the deceleration and the eventual reflection of the low energy ions within the sheath, as already discussed in section 2.3.1.

4.2. The equivalent circuit solver

The presence, in a typical plume-SC interaction, of several conductive walls with non-local boundary conditions,

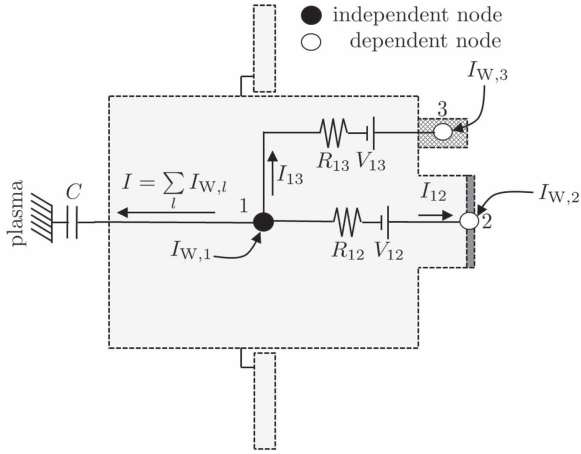


Figure 4. Scheme of the equivalent circuit, for a simulation featuring three different conductive objects.

complicates the integration of the time-dependent equations. As with other existing plume–S/C interaction codes [27], an efficient way to overcome that difficulty is to add an equivalent electric circuit linking the different walls of the problem and the plasma. Figure 4 illustrates this numerical scheme. Each conductive object l is assumed to be an iso-potential node, receiving a current from the plasma $I_{W,l}$ (indeed, equation (28)) and connected to another iso-potential node m by means of both a resistance R_{lm} , and a forced voltage bias V_{lm} .

One of the nodes (the S/C node in figure 4) is considered as independent and its potential relative to the plasma reference point (with $\phi = 0$) is first computed as the time evolution of the voltage of an equivalent capacitor C ,

$$\frac{d\phi_1}{dt} = \frac{I}{C}, \quad (29)$$

where the charging current I is obtained as the sum of the plasma currents to the circuit nodes $I = \sum_l I_{W,l}$. In the steady state, I must be zero and ϕ_1 is the floating potential of the S/C. Kirchhoff laws then yield:

$$\begin{cases} \text{current continuity at dependent node } l: & I_{W,l} + \sum_{m \neq l} I_{ml} = 0, \\ \text{potential across connection } lm: & \phi_l - I_{lm} R_{lm} + V_{lm} - \phi_m = 0. \end{cases} \quad (30)$$

For the case in figure 4, there are two dependent nodes and two connections. Equation (30) thus determine the two unknown dependent node potentials and internode currents. Values of R_{lm} , V_{lm} and C are selected based on either real electrical properties of the S/C parts or to facilitate numerical convergence.

5. Treatment of non-neutral regions

Once the quasineutral solution for the electron density n_e^* , the electric potential ϕ^* , and the electron temperature T_e^* are known at the instant $t^{(k)}$, the simulation domain is dynamically split into

quasineutral and non-neutral subdomains, and the solution at time $t^{(k)}$ is recomputed in the non-neutral subdomain.

First of all, the quasineutral subdomain, constituted by quasineutral nodes and boundary faces, must be defined. We will consider that cells and boundary faces are quasineutral if their level of non-neutrality is below a maximum value, called ϵ_{\max} (a value of 0.032 is considered later in the simulations, which corresponds to a relative charge density of 1‰). For inner cell nodes, non-neutrality is measured by

$$\epsilon_n = \left| \frac{\epsilon_0 \nabla^2 \phi^*}{en_e^*} \right|^{1/2} = \left| \frac{n_e^* - n_e}{n_e^*} \right|^{1/2}, \quad (31)$$

and the cell node is part of the non-neutral subdomain when $\epsilon_n > \epsilon_{\max}$. For material boundary faces, non-neutrality is measured by the ratio between the local Debye length and the cell size Δl (in the direction normal to the surface):

$$\epsilon_f = \frac{1}{\Delta l} \sqrt{\frac{\epsilon_0 T_e^*}{e^2 n_e^*}}. \quad (32)$$

Now it must be decided whether a discontinuity sheath is postulated at the boundary of the simulation domain (which we will call S) or this boundary is already the wall W. Numerical convergence between these two cases demands the addition of an intermediate case. Therefore, three cases are considered:

- if $\epsilon_f \geq 1$: the boundary face is non-neutral, the sheath is directly simulated inside the plasma domain, and the boundary face is the wall, i.e. $\phi_S = \phi_W$,
- if $\epsilon_f \leq \epsilon_{\max}$: the boundary face is quasineutral, the sheath is treated separately as a discontinuity, and the potential at S is the quasineutral sheath edge potential ϕ_S^* ,
- if $\epsilon_{\max} < \epsilon_f < 1$, a partial sheath is added outside the plasma domain, with a potential drop given by:

$$\phi_S - \phi_W = \frac{1 - \epsilon_f}{1 - \epsilon_{\max}} (\phi_S^* - \phi_W), \quad (33)$$

where ϕ_S^* and ϕ_W are known, respectively, from the quasineutral solution and the current wall potential.

We point out that for computational purposes, equations (31) and (32) are always estimated at the mesh nodes. Once the non-neutral subdomain is defined, the Poisson equation, equation (14), and equation (23) for the Bernoulli function should be integrated simultaneously to determine ϕ and the electron fluid magnitudes at these mesh nodes. This is particularly costly computationally, so a different approach is proposed here. First, we assume that $\partial \rho_c / \partial t \ll \nabla \cdot \mathbf{j}_d$ (i.e. we focus on quasi-steady solutions) and we propose to obtain H_e from equation (25) with the substitutions

$$\sigma_e^* \rightarrow \sigma_e^{(k-1)}, \quad \mathbf{j}_d^* \rightarrow \mathbf{j}_d^{(k-1)}. \quad (34)$$

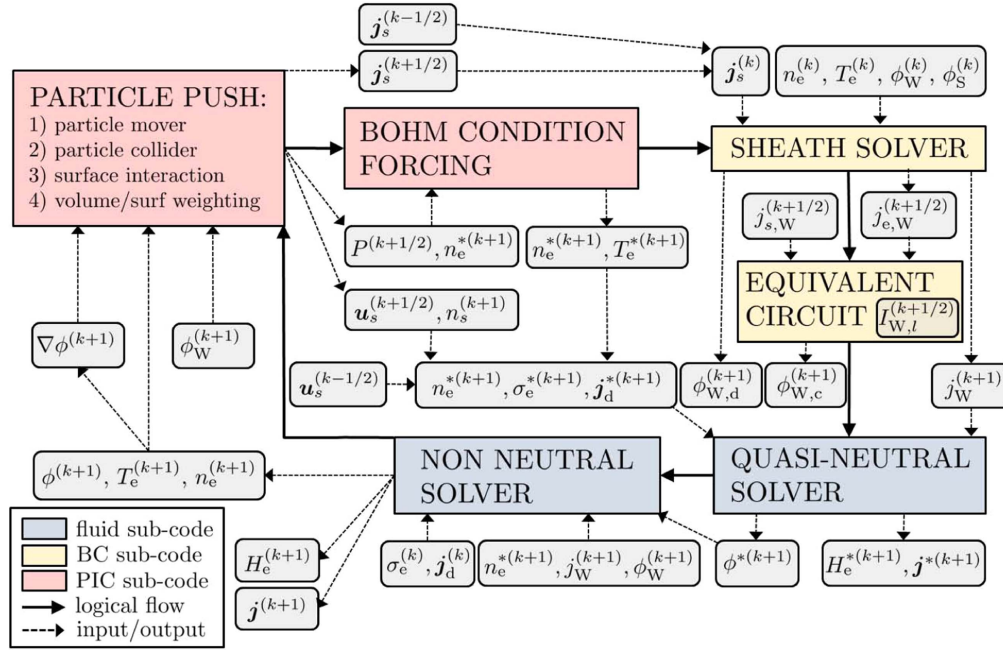


Figure 5. The hybrid-particle code simulation loop at time step $k + 1$ (from time $t^{(k)}$ to time $t^{(k+1)}$).

Then, from equations (21) and (22), one has (for the generic polytropic case)

$$n_e(H_e, \phi) = n_{e0} \left[1 + \frac{\gamma - 1}{\gamma} \frac{H_e + e\phi}{T_{e0}} \right]^{\frac{1}{\gamma-1}}, \quad (35)$$

which, substituted into the Poisson equation, yields a nonlinear equation for ϕ ,

$$\frac{\epsilon_0}{e} \nabla^2 \phi = n_e(H_e, \phi) - n_e^*. \quad (36)$$

The numerical procedure to solve this equation is explained in appendix B.

6. The overall simulation loop

A generic step of the overall simulation loop is shown in figure 5 for a general non-neutral simulation. The particle push represents several PIC algorithms and generates updated fluid properties at times $k + 1$ (quasineutral electron density n_e^* , and heavy particle densities n_s) and $k + 1/2$ (heavy particle fluid velocities u_s , and surface weighted variables at material boundaries). The quasineutral electron density and the surface weighted P variable are then fed to the Bohm condition-forcing algorithm, which corrects, if need be, the value of the electron density at the quasineutral material boundaries, thus completing the PIC sub-step.

Then, boundary conditions for the fluid closure at this new time $k + 1$ need to be updated. First, the sheath solver updates the electron current density $j_{e,W}$ at conductive walls, and the dielectric wall potential $\phi_{W,d}$ both at time k , since its inputs (wall potential, sheath edge potential, electron density, temperature, and ion current) are known at this time step. The electron current density is then extrapolated to time $k + 1/2$ and passed together

with the ion current density to the wall $j_{i,W}$ (at time $k + 1/2$) to the equivalent circuit solver. This obtains the electric current $I_{W,l}^{(k+1/2)}$ to the conductive objects and updates their potentials to time $k + 1$, with a second-order leap-frog scheme. The sheath solver also extrapolates the dielectric wall potential and the total electric current density to the wall $j_W = j_{e,W} + j_{i,W}$ to time $k + 1$, as needed by the fluid closure algorithms.

This is then fed, together with the quasineutral electron density n_e^* , conductivity σ_e^* , and driving current density j_d^* , all at time $k + 1$, to the quasineutral solver, which solves for the quasineutral electric potential ϕ^* , the Bernoulli function H_e^* , and the electric current density j^* at time $k + 1$. The non-neutral solver then receives, as input, the quasineutral potential ϕ^* , the wall potential ϕ_W , and the quasineutral density n_e^* at time $k + 1$, and assumes the latest step values for σ_e and j_d . Its outputs are the electric potential ϕ , electron temperature T_e , density n_e and Bernoulli function H_e at the time step $k + 1$. These, together with the updated wall potentials at time $k + 1$, are fed back to the PIC model and the next time step is finally initiated.

The exact time consistency described above allows us to achieve a second-order accuracy in the time integration. However, a commonly used approach, that helps reduce the numerical noise and is considered in the simulations of section 7, is to use time-averaged properties at the material boundaries (as already mentioned in section 2.3.2), with a number of averaging steps in the order of 50–100 ($\Delta k_{\text{avg}} = 100$ in the presented simulations).

7. Simulations

7.1. Definition of the simulation geometry and settings

The plume–S/C interaction scenario considered for the model validation features a cubic S/C with an ion thruster, a hollow

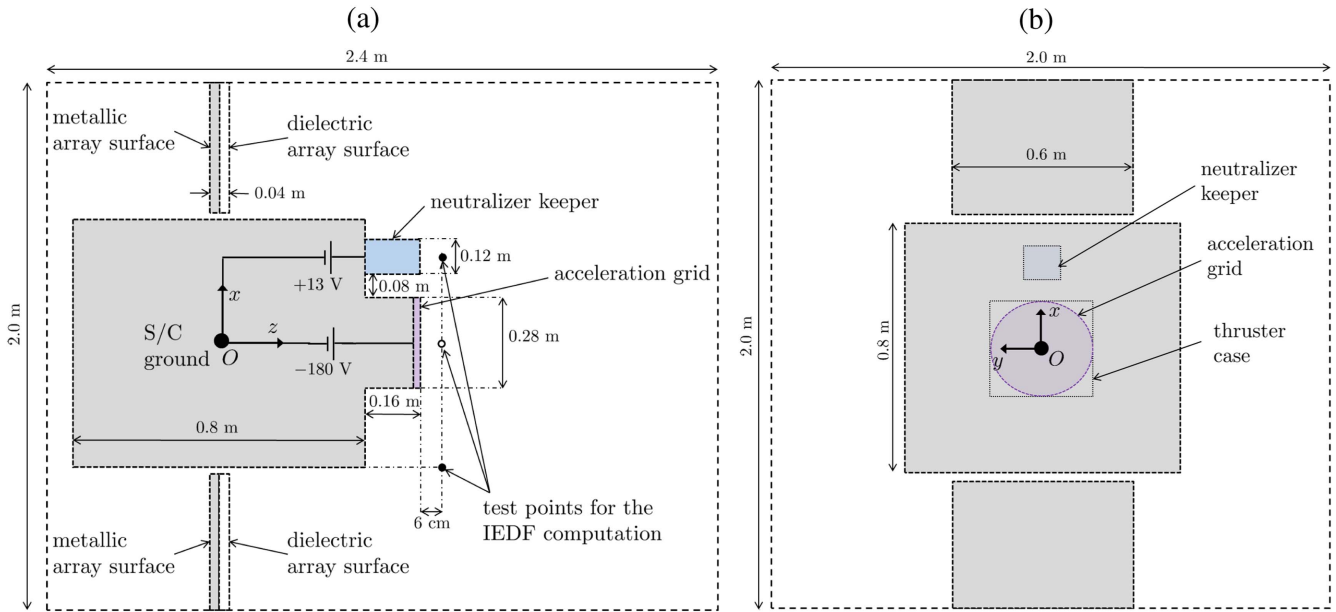


Figure 6. Simulation domain for the S/C–plume interaction scenario: (a) $x - z$ cross-section, and (b) $x - y$ cross-section, both through the satellite center. The PIC mesh is Cartesian, with a number of nodes along x , y , and z of $101 \times 101 \times 121$ (2 cm side cells). The white dot on the thruster symmetry axis is the reference point for the electron properties, the electric potential, and the Bernoulli function. Two additional points on the thruster side and on the neutralizer axis are considered for the computation of the ion energy distribution function (IEDF).

Table 3. Considered parameters for the plasma–plume satellite interaction simulation. Applied voltages refer to the S/C ground. All considered objects are conductive, except for the front surface of the solar arrays, which is dielectric.

Simulation parameter	Units	Values
Neutralizer keeper voltage	V	+13
Acceleration grid voltage	V	−180
Thruster mass flow rate	sccms	27.13
Thruster mass utilization efficiency	%	90.0
Doubly to singly charged ion current ratio	%	9.1
Injected Xe^+ profile (thruster)	n/a	SSM ($R_0 = 14$ cm, and $\alpha_0 = 20.5$ deg)
Injected Xe^{++} profile (thruster)	n/a	SSM ($R_0 = 14$ cm, and $\alpha_0 = 30$ deg)
Injected Xe^+ energy (thruster)	eV	1040
Injected Xe^{++} energy (thruster)	eV	2080
Injected Xe^+ temperature (thruster)	eV	0.1
Injected Xe^{++} temperature (thruster)	eV	0.2
Injected neutrals profile (thruster)	n/a	Flat
Injected neutrals velocity (thruster)	m/s	247 (sonic)
Injected neutrals temperature (thruster)	eV	0.05
Neutralizer mass flow rate	sccms	3.59
Injected neutrals profile (neutralizer)	n/a	Flat
Injected neutrals velocity (neutralizer)	m/s	247 (sonic)
Injected neutrals temperature (neutralizer)	eV	0.05
Neutralizer ion flow percentage	%	5.0
Injected Xe^+ , Xe^{++} profile (neutralizer)	n/a	Thermal, Gaussian ($R_0 = 4$ cm)
Injected Xe^+ temperature (neutralizer)	eV	0.2
Injected Xe^{++} temperature (neutralizer)	eV	0.4
Electron temperature at thruster exit	eV	3.5
Electron polytropic cooling coefficient	n/a	[1.0, 1.3]

cathode neutralizer, and two solar arrays, as shown in figures 6(a) and (b), while the corresponding equivalent circuit is shown in figure 4.

Three conductive objects are considered: the satellite ground (including cubic body, thruster case and the back-face

of the solar arrays), the neutralizer keeper external surface, and the most external grid of the thruster. The resistances between the S/C ground and acceleration grid and neutralizer keeper are assumed to be zero ($R_{12} = R_{13} = 0$). The front face of the solar arrays, as shown in figure 6(a), is modeled as a

dielectric object (i.e. the wall potential is determined locally from the current equilibrium).

The values of some simulation parameters are summarized in table 3. The considered thruster simulates the NASA's NSTAR ion thruster [74, 75], while the applied voltages to the acceleration grid and neutralizer keeper are kept constant to, respectively, $V_{12} = -180$ and $V_{13} = +13$ V. The negative grid potential prevents most of the electrons from back-streaming towards it, while the neutralizer keeper is biased positive with respect to the S/C ground [75].

The injection areas for both the thruster and neutralizer are circular with radii of respectively 14 and 4 cm. Neutrals are injected axially with sonic conditions and with a flat density profile from both the thruster and neutralizer injection cells. Regarding the thruster ions, these are injected following a self-similar profile [13, 17], with an outermost streamline divergence angle $\alpha_0 = 20.5$ deg (at the radius $R_0 = 14$ cm from the thruster centerline). This divergence profile corresponds to a divergence efficiency of 0.98, as considered in [75]. An already developed divergence angle is considered because the mesh is not fine enough to simulate the effects of beamlet injection and coalescence into a single beam, so that the injection surface is actually simulated as a quasineutral surface, with a thin sheath (across which the potential drops from its value at the quasineutral plasma to that of the acceleration grid). Regarding the neutralizer ions, past studies [76] have shown that a significant ion current is also emitted. Here, we have considered that 5% of the total mass flow of the neutralizer is emitted in the form of singly or doubly charged ions from a thermal reservoir (with a temperature of 0.2 and 0.4 eV respectively). Finally, a ratio between the doubly and singly charged ion current of 9.1% [77] has been considered for both the thruster and the neutralizer emissions.

Regarding the electron thermodynamics, a peak electron temperature of 3.5 eV, consistent with existing experimental measurements for similar thrusters [78], is assumed at a node located 6 cm downstream from the thruster exit (which represents the reference plasma point for the potential, Bernoulli function and electron enthalpy), while four different values for γ are considered: 1.0 (isothermal), 1.1 (reference case), 1.2 and 1.3.

Regarding the applied fluid closure, the simulations are run with the sole quasineutral solver between $t = 0$ and $t = 1$ ms, and, starting from $t = 1$ ms, the non-neutral solver is activated. The requested time for a slow CEX ion (with an energy content of 5 eV) to cross the entire simulation domain is around 1 ms, so that the considered simulation time is expected to be sufficient to reach stationary conditions.

The boundary conditions for the computation of the Bernoulli function H_e , for this simulation setup, are:

- Current free condition $\mathbf{j} \cdot \mathbf{1}_\perp = 0$ at the external boundaries and at the dielectric walls of the solar array front surface, thus yielding:

$$\frac{\partial H_e}{\partial \mathbf{1}_\perp} = -\frac{e}{\sigma_e} \mathbf{j}_d \cdot \mathbf{1}_\perp.$$

- Fixed electric current $j_w = j_w(\phi_w)$ to the other conductive walls:

$$\frac{\partial H_e}{\partial \mathbf{1}_\perp} = \frac{e}{\sigma_e} (j_w - \mathbf{j}_d \cdot \mathbf{1}_\perp).$$

- Dirichlet conditions $H_e = \text{const}$, at the emissive surface of the neutralizer, equivalent to leaving a free electron current to balance the electron current lost to the boundaries, and generated inside the domain (e.g. due to ionization).

Regarding the electric potential, the boundary conditions (already discussed above) are:

- Dielectric or conductive wall potential $\phi = \phi_w$ at the non-neutral material boundary nodes.
- Transition conditions $\phi = \phi_s$ (refer to equation (33)) at the transition material boundary nodes.
- Quasineutral electric potential $\phi = \phi^*$ at all quasineutral nodes (including those on the external boundary).
- $\phi = 0$ at the reference node for the electron properties (6 cm downstream from the thruster exit area, on its axis).
- Neumann conditions on ϕ at the non-neutral external boundary nodes:

$$\frac{\partial \phi}{\partial \mathbf{1}_\perp} = 0.$$

7.2. Discussion of the simulation results

The simulation results for the reference simulation case ($\gamma = 1.1$) are shown in figures 7(a)–(h). The electric potential is shown in figure 7(a). The S/C is floating at a potential of -38 V with respect to the plasma plume near the thruster exit (the reference potential point is shown by a white dot), so that the iso-potential lines adapt to this value close to the cubic S/C body through spatially resolved plasma sheaths. The effect of the CEX ions is clearly visible on the left of the main plasma plume, while the neutralizer creates a plasma bridge with the thruster (necessary for the plume current neutralization) and substantially alters the symmetry of the plasma response.

The electron density is shown in figure 7(b), and closely follows the evolution of the electric potential, with densities rapidly dropping to zero as the very negative S/C surfaces are approached. On the lateral sides of the thruster, the electron density nearly coincides with the CEX ion density and shows values between 10^{12} m^{-3} and 10^{13} m^{-3} , a result which is consistent with the simulation results and experimental measurements of past studies of the same thruster, such as those of [79, 80], and [81].

The electric current density is shown in figure 7(c). A virtually current-free plasma plume is achieved just 30–40 cm

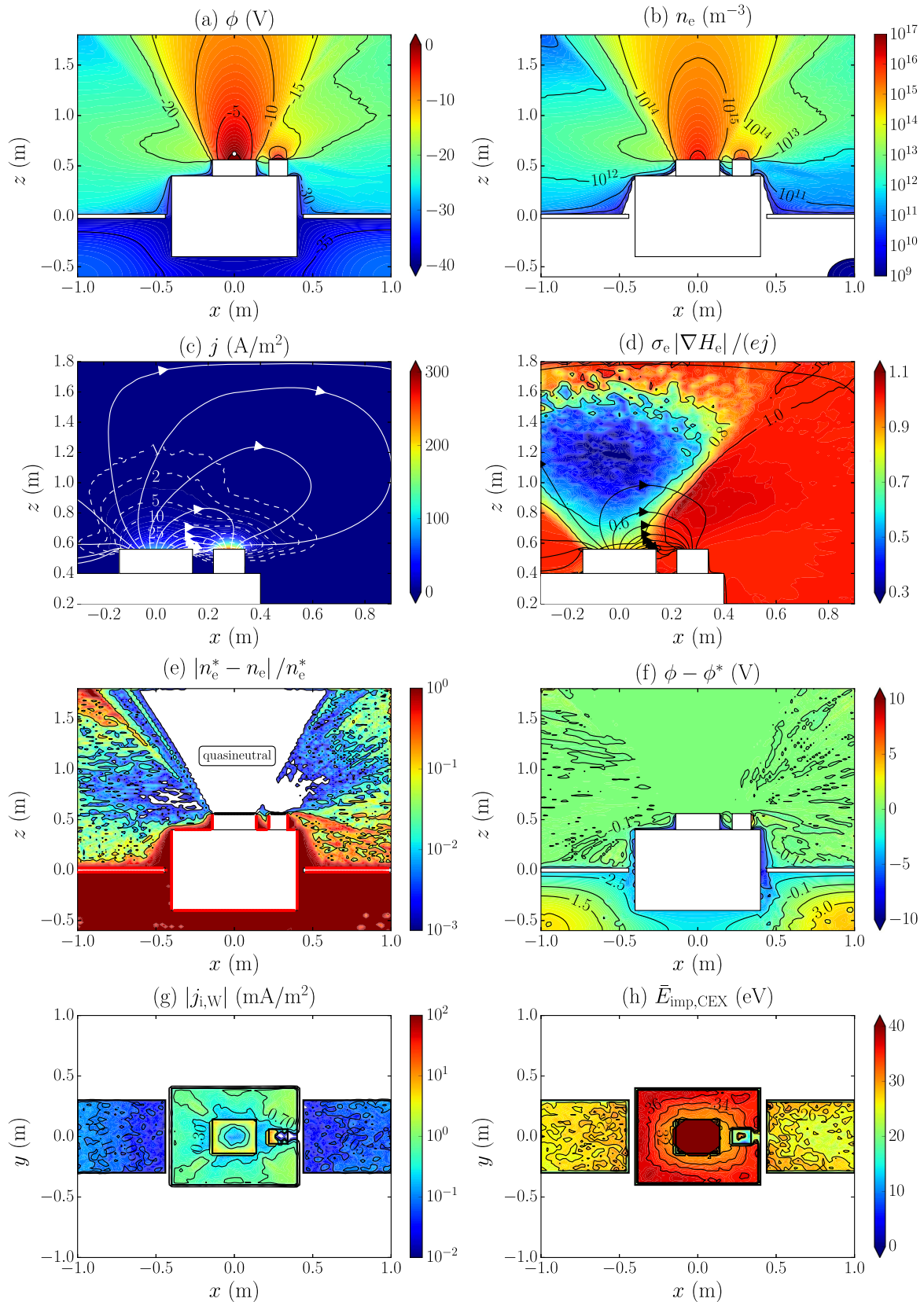


Figure 7. Simulation results for the reference case with $\gamma = 1.1$: (a) electric potential (reference point is shown with a white dot), (b) electron density, (c) electric current density and streamlines, (d) relative contribution of $\sigma_e |\nabla H_e| / e$, (e) non neutrality ratio or ε_n^2 , (f) difference on the electric potential between the non-neutral and quasineutral solvers, (g) total ion current density to the S/C front walls, and (h) average ion wall-impact energy on the S/C front walls. Subplots (a)–(f) refer to the $y = 0$ cross section, while subplots (g) and (h) refer to the front surfaces of the thruster case, neutralizer, S/C cubic body and solar arrays.

downstream from the thruster exit, which is consistent with the assumption that the far-region plasma is essentially current free. All electric current streamlines originate at the thruster exit (due to the emitted ions) and reach the neutralizer emission surface (due to emitted electrons) just as expected (no electric current sources exist inside the domain). The total electric current is given by Ohm's law, equation (20), and presents two different contributions: the product $\sigma_e \nabla H_e / e$ and the driving current \mathbf{j}_d . The clearly dominating term is the former, as shown in figure 7(d), showing its relative magnitude (normalized with the electric current density) and streamlines. In fact, although the absolute potential correction H_e is almost negligible (the plasma is lowly collisional) and in the order of a few mV, the electron conductivity is quite high, presenting values around $3000 \Omega^{-1} \text{m}^{-1}$ at the thruster exit (slowly decreasing along the plume centerline due to the expansion), and two local peaks of approximately $1000 \Omega^{-1} \text{m}^{-1}$ at the neutralizer exit, where ions are emitted and the quasineutral plasma density is locally large, and around the plume core, where the ratio between the CEX ion and the neutral densities reaches a local maximum. The only region in which the driving term \mathbf{j}_d is comparable in magnitude to $\sigma_e \nabla H_e / e$ is the central region of the main plasma plume, where it accounts for approximately half of the total electric current density.

Regarding the simulation domain sub-division into quasineutral and non-neutral regions, this is shown in figure 7(e), showing the normalized charge density (ϵ_n^2 in equation (31)). The white regions correspond to the quasineutral subdomain, featuring a normalized charge density (in absolute value) lower than 1%. Regarding the S/C walls, these are all non-neutral, with the injection areas of the thruster and neutralizer being the only quasineutral boundary surfaces. The difference in potential due to the solution of the non-neutral regions (with the Poisson solver) is finally shown in figure 7(f). The largest differences between the non-neutral and neutral solver solutions are found close to the S/C surfaces and reach values around 10 V (with the non neutral solution being more negative).

An important capability of a S/C–plasma interaction tool is to predict the ion current flux to the S/C walls, and the ion mean wall-impact energy (to evaluate the effects of sputtering and deposition). Figure 7(g) shows the ion current density reaching the S/C front surfaces (the absolute value of $j_{i,w}$). A maximum ion current density of up to 10 mA m^{-2} is reached at the corners of the thruster case and on one side (the one closer to the thruster) of the neutralizer keeper. The average current density to the S/C cubic body is around 0.5 mA m^{-2} . The current density to the solar array, on the other hand, is generally lower than 0.1 mA m^{-2} . Figure 7(h) finally shows the average wall-impact kinetic energy of the ions hitting the S/C walls. This is in the order of 30–35 eV at the S/C cubic body front surface, and lower than 30 eV at the solar arrays. These values depend mostly on the floating potential of the S/C with respect to the plasma plume denser region (where most of the CEX ions are generated).

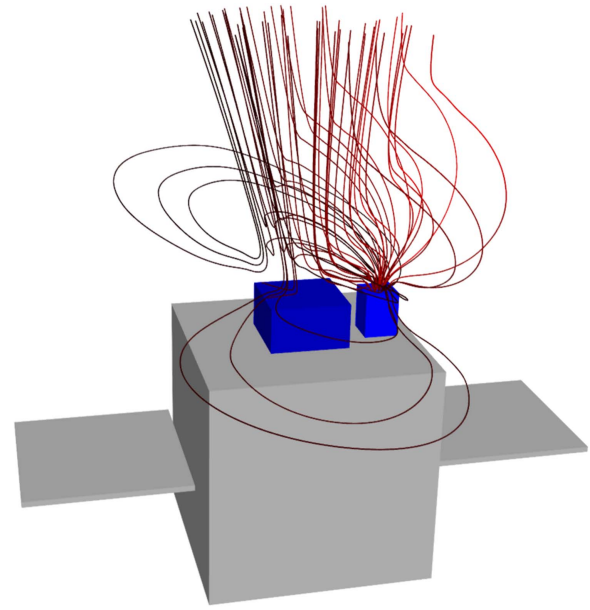


Figure 8. 3D electron streamlines emanating from the neutralizer and merging with the ion plume. The farther (from the neutralizer) the ion streamline to be neutralized, the darker the color of the corresponding electron streamline. Please note that the electron streamlines do not represent the electron trajectories.

The 3D streamlines of the electron current density (which are not the electron trajectories) are then shown in figure 8. The farthest (from the neutralizer) conical plume streamlines are neutralized by electrons that circle around the dense region of the plume. This behavior can be justified by the fact that electrons tend to follow the minimum resistance path. So, instead of neutralizing the plume by directly crossing the thruster front face at right angles (which would yield large collision losses with the emitted ions and neutrals), they take advantage of the high conductivity peripheral plasma populated by CEX ions (which feature a very low neutral density). A final observation is that all electron streamlines originate from the emission surface of the neutralizer keeper, because $\nabla \cdot \mathbf{j}_e \approx 0$ inside this lowly collisional plasma (ionization effects are almost negligible).

The ion energy distribution function [82] at the three test points of figure 6(a) is shown in figure 9(a). Close to the thruster exit (black solid line), three well-defined populations of ions can be identified: the emitted doubly charged ions (with energies around 2080 eV), the emitted singly charged ions (with energies around 1040 eV), and the slow CEX ions (including both singly and doubly charged ions), which feature energies that are generally below 3eV. On the thruster side (dotted blue line), on the other hand, only CEX ions are present, and the singly and doubly charged ion populations can be distinguished again in terms of energy content. In fact, the energy of these ions depends directly on the potential difference between the location where they are generated (dense plume region, with $\phi \in [0, -5]$ V) and the considered point potential ($\phi \approx -20$ V). Finally, at the neutralizer axis, the emitted singly and doubly charged ions can be clearly distinguished from CEX ions generated in the plume: the two

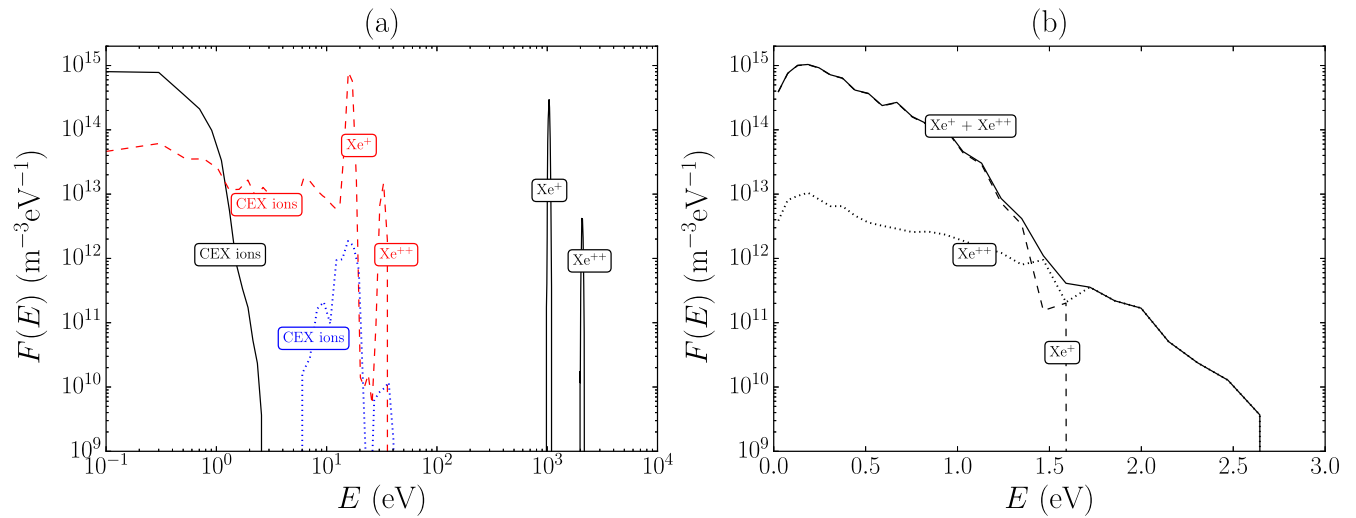


Figure 9. (a) Ion energy distribution function at three different locations, shown in figure 6(a): thruster axis (black solid line), neutralizer axis (red dashed line), and 40 cm off the thruster axis, opposite to the neutralizer position (blue dotted line). (b) Zoom of the slow CEX ions distribution function at the thruster axis: total (solid line), singly charged (dashed line), and doubly charged (dotted line) contributions. All results are instantaneous and not time averaged.

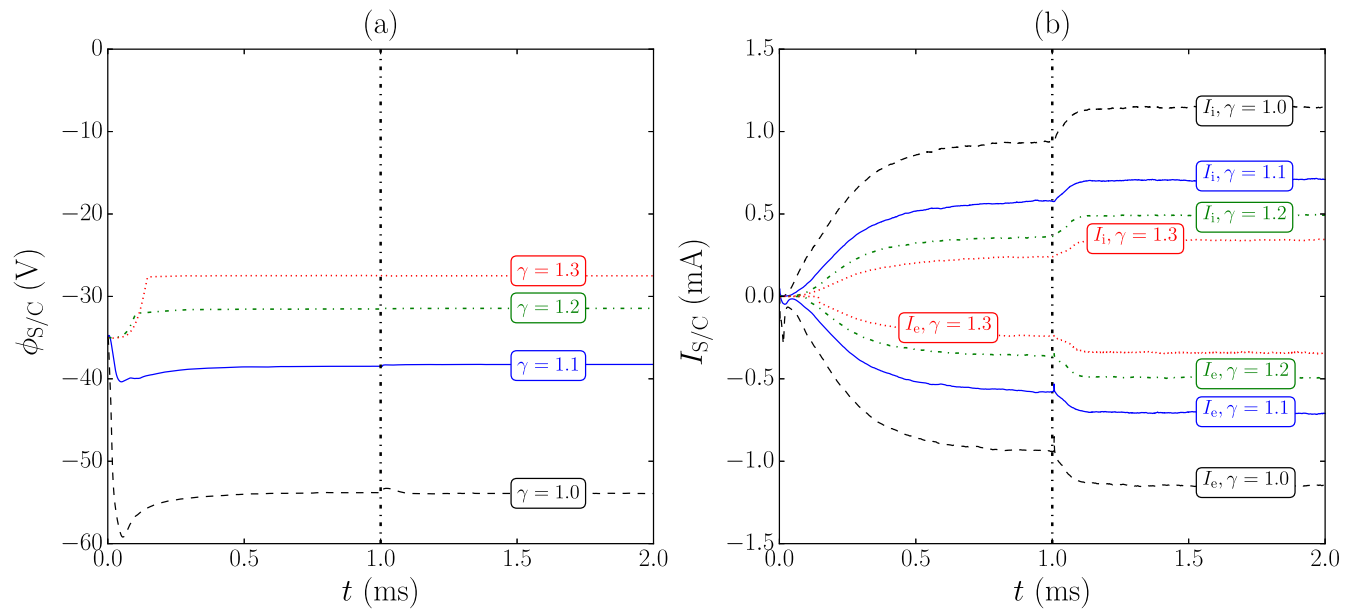


Figure 10. Time averaged evolutions (over 100 steps) of (a) S/C potential and (b) electron and ion current to the S/C walls (including thruster grid and case, neutralizer and solar arrays) for the different γ cases: isothermal (black dashed line), $\gamma = 1.1$ (blue solid line), $\gamma = 1.2$ (green dash-dot line), and $\gamma = 1.3$ (red dotted line). A vertical dash-dot line indicates when the non-neutral solver is activated ($t = 1$ ms).

well-defined peaks at energies of approximately 15 and 30 eV are indeed caused by the acceleration of the emitted ions due to the ambipolar electric field at the neutralizer exit (characterized by a step potential drop). Finally, a zoom of the ion energy distribution function at the thruster axis is shown in figure 9(b), which also provides the separate contributions of singly and doubly charged ions. The disparity of energies and distributions of the different ion populations shown in figures 9(a) and (b) clearly makes the use of multiple fluids for the ion species challenging.

The electron thermodynamics affects both the equilibrium S/C potential and the total current (due to ions and

electrons) to the S/C walls (including thruster grid, neutralizer and solar arrays), as shown in figures 10(a) and (b). After a short transient, the electric potential of the S/C reaches a stationary value, which means that the total current to the S/C node (I in figure 4) approaches zero or fluctuates dimly around it. Moreover, the floating potential is quite stable for all γ cases (the chosen value for the charging capacity C is 20 nF).

The larger the polytropic coefficient, the less negative the S/C floats, as suggested by the limit to which the electric potential tends when the electron density goes to zero, which is $-\gamma T_{e0}/(e(\gamma - 1))$, as shown in [12, 13]. Clearly, since the

collected electron current is affected by this limit, the floating potential of the S/C also adapts to it. Moreover, the closer the electrons are to isothermal, the larger the collected ion and electron currents because of the larger electric fields that are capable of deviating a larger fraction of slow ions towards the S/C. The transition from the (only) quasineutral solution to a non neutral one is also clear in figure 10(b), where a sudden increase of up to 20% in the collected ion/electron current is registered when activating the non-neutral solver (at $t = 1$ ms). Therefore, solving the finite non-neutral plasma sheaths that surround the S/C has a non-negligible influence on the ion flux impinging the S/C.

8. Conclusions

This paper has presented a highly flexible 3D hybrid model to study the current neutralization and the interaction of a plasma plume with any nearby object, featuring:

- A weakly-collisional electron model admitting a polytropic fitting for the electron pressure tensor, which allows us to obtain both the corrected electric potential (due to collisional effects) and the electric current density in the plume.
- An adaptive algorithm that splits the simulation domain into quasineutral and non-neutral regions and handles a smooth transition between them. While, in the former, the fluid closure relies on the sole electron momentum balance equation, in the latter, this is coupled with the Poisson equation.
- A correct transition between quasineutral material boundaries, where the Bohm condition is applied, and non-neutral spatially-resolved plasma sheaths.
- Use of both volumetric and surface weighting algorithms for, respectively, the inner mesh nodes and the boundary faces.
- Treatment of CEX collisions with a DSMC approach, which also allows us to track the fast neutrals.
- Macro-particle population control, based on a generation macro-particle weight, to limit the statistical noise of the PIC algorithms.

A benchmark simulation has then allowed us to validate the code, showing that results for the CEX ion density are definitely consistent with the available data in the literature. Moreover, it has highlighted that both the electron thermodynamics and the non-neutral plasma regions play a non-negligible role in determining the ion flux impinging the S/C. Regarding the former, the closer the electrons are to isothermal, the higher this flux and the average wall-impact energy, and the lower the S/C floating potential. A significant backscattered CEX ion flux increase is systematically found when switching from a quasineutral solution to a non-neutral one.

Future developments of the model and code should tackle the following aspects:

- New heavy particle collisions, such as the momentum exchange collisions between ions and neutrals (MEX).
- A new wall type characterized by the sputtering of both neutral and charged material particles.
- A more effective population control to deal with plume expansion effects. This should feature, on top of the already existing control, a particle renormalization algorithm.
- An extension of the electron model to magnetized plasma plumes in order to study the distortion effects caused by any applied external magnetic field (such as the geomagnetic field) on the plume expansion.

Acknowledgments

The research leading to the results of this paper was initiated within the *LEOSWEEP* project ('Improving Low Earth Orbit Security With Enhanced Electric Propulsion'), funded by the European Union Seventh Framework Programme (FP7/2007-2013) under grant agreement N.607457. Additional funding to complete it has been received by Spain's R&D National Plan, under grant ESP2016-75887.

Appendix A. Models for collisions

A.1. CEX cross section

The CEX cross section for both types of CEX reactions (singly and doubly charged ions with neutrals) is provided, for xenon gas, by the Miller model [15]:

$$\sigma(v_i) = C_1 - C_2 \cdot \log_{10} \left(\frac{1/2 m v_i^2}{1 \text{ eV}} \right), \quad (37)$$

where the argument of the logarithm represents the relative kinetic energy of the impacting elementary particles, expressed in eV. The constants depend on the type of reaction:

- $\text{Xe}^+(\text{fast}) + \text{Xe}(\text{slow}) \rightarrow \text{Xe}^+(\text{slow}) + \text{Xe}(\text{fast})$:
 $C_1 = 87.3 \text{ \AA}^2$, $C_2 = 13.6 \text{ \AA}^2$
- $\text{Xe}^{++}(\text{fast}) + \text{Xe}(\text{slow}) \rightarrow \text{Xe}^{++}(\text{slow}) + \text{Xe}(\text{fast})$:
 $C_1 = 45.7 \text{ \AA}^2$, $C_2 = 8.9 \text{ \AA}^2$

A.2. Electron collision frequency

In order to compute the electron momentum transfer collision frequency with the s^{th} particle population ν_{es} , only elastic collisions are taken into account. The electron-ion collision frequencies are then obtained as [83]:

$$\nu_{es} = \frac{2^{1/2} n_s Z_s^2 e^4 \ln \Lambda}{12 \pi^{3/2} \epsilon_0^2 m_e^{1/2} T_e^{3/2}}, \quad (38)$$

where n_s is the s^{th} population number density, and the parameter $\ln \Lambda \approx 10$. For the neutrals, on the other hand, the collision frequency is computed by integrating the elastic

collision cross section $\sigma_{es}(v_e)$ over a Maxwellian electron distribution function [84, 85]:

$$\nu_{es} = n_s \sqrt{\frac{2T_e}{9\pi m_e}} \int_0^\infty x^5 \sigma_{es}(x) \exp\left(-\frac{x^2}{2}\right) dx, \quad (39)$$

where $x = v_e/c_e$ represents the normalized electron velocity with respect to the electron thermal velocity $c_e = \sqrt{T_e/m_e}$, and $\sigma_{es}(x)$ depends on the s^{th} population atomic type, and follows the model of [86] (for xenon). It can be noticed that equations (13), (38) and (39) are only valid if the electron thermal velocity c_e is much larger than the fluid velocities of both the heavy particle population u_s and of the electrons u_e .

Appendix B. Solving the non-linear Poisson equation

Since the electron density is an explicit function $n_e = n_e(\phi, H_e)$, of both the known Bernoulli function and unknown potential, equation (14) becomes a non-linear differential equation in ϕ . In numerical form, if ϕ_l is the unknown potential at the l^{th} mesh node, then the l^{th} non-linear system equation can be written as:

$$f_l = \sum_{m \in \text{mesh}} A_{lm} \phi_m + \frac{e}{\epsilon_0} (n_{e,l}^* - n_{e,l}(\phi_l, H_{e,l})) = 0, \quad (40)$$

where the summation extends to all mesh nodes, $n_{e,l}^*$ is the known quasineutral electron density at node l , and A_{lm} is the (l, m) element of the sparse coefficients matrix.

Equation (40) can be solved iteratively with a Newton–Raphson method by linearizing it around the current solution for the electric potential $\phi^{(k)}$, with k now representing the iteration step. The initial estimate $\phi^{(0)}$ is given by either the quasineutral electric potential ϕ^* (at the very first simulation step), or by the previous time step solution (at other simulation steps). The linearization proceeds by evaluating the Jacobian matrix of the non-linear system, at the iteration step k , as:

$$J_{lm}^{(k)} = \left. \frac{\partial f_l}{\partial \phi_m} \right|_{\phi=\phi^{(k)}}, \quad (41)$$

and then obtaining the electric potential correction $\Delta\phi^{(k)}$ by solving the linearized system:

$$\sum_{m \in \text{mesh}} J_{lm}^{(k)} \Delta\phi_m^{(k)} = -f_l^{(k)}. \quad (42)$$

The new electric potential, for the next iteration step $k + 1$, is updated as $\phi_l^{(k+1)} = \phi_l^{(k)} + \Delta\phi_l^{(k)}$ and used to update the Jacobian matrix. This iterative scheme is repeated until a convergence criterion is met, i.e. until the maximum absolute value of the non linear function f is below a user’s defined tolerance.

ORCID iDs

Filippo Cichocki <https://orcid.org/0000-0003-4768-9397>
 Adrián Domínguez-Vázquez <https://orcid.org/0000-0003-3935-7333>

Mario Merino <https://orcid.org/0000-0001-7649-3663>
 Eduardo Ahedo <https://orcid.org/0000-0003-2148-4553>

References

- [1] Goebel D M and Katz I 2008 *Fundamentals of Electric Propulsion: Ion and Hall Thrusters* (Pasadena, CA: Jet Propulsion Laboratory)
- [2] Ahedo E 2011 Plasmas for space propulsion *Plasma Phys. Control. Fusion* **53** 124037
- [3] Garrett H B 1981 The charging of spacecraft surfaces *Rev. Geophys.* **19** 577–616
- [4] Boyd I D and Ketsdever A 2001 Interactions between spacecraft and thruster plumes *J. Spacecr. Rockets* **38** 380–380
- [5] Bombardelli C and Peláez J 2011 Ion beam shepherd for contactless space debris removal *J. Guid. Control Dyn.* **34** 916–20
- [6] Bombardelli C, Urrutxua H, Merino M, Ahedo E and Peláez J 2012 *Relative dynamics and control of an ion beam shepherd satellite Proc. of the AAS/AIAA Space Flight Mechanics Meeting 2012* (Univelt, Inc.) pp 2145–58
- [7] Bombardelli C, Urrutxua H, Merino M, Ahedo E and Peláez J 2013 The ion beam shepherd: a new concept for asteroid deflection *Acta Astronaut.* **90** 98–102
- [8] Merino M, Ahedo E, Bombardelli C, Urrutxua H and Peláez J 2013 Ion beam shepherd satellite for space debris removal *Progress in Propulsion Physics EUCASS Advances in Aerospace Sciences* vol 4 (*Les Ulis*) (EDP Sciences) pp 789–802
- [9] Lieberman M A and Lichtenberg A J 2005 *Principles of Plasma Discharges and Materials Processing* (Hoboken, NJ: Wiley)
- [10] Wilhelm K et al 2011 Morphology, dynamics and plasma parameters of plumes and inter-plume regions in solar coronal holes *Astron. Astrophys. Rev.* **19** 35
- [11] Mascali D, Tudisco S, Bonanno A, Gambino N, Ivanovski S, Anzalone A, Gammino S, Miracoli R and Musumeci F 2010 Colliding laser-produced plasmas: a new tool for nuclear astrophysics studies *Radiat. Eff. Defects Solids* **165** 730–6
- [12] Cichocki F, Merino M and Ahedo E 2014 Modeling and simulation of EP plasma plume expansion into vacuum *50th Joint Propulsion Conf. (Cleveland, OH, July 28–30 2014)* (Reston, VA: AIAA)
- [13] Merino M, Cichocki F and Ahedo E 2015 Collisionless plasma thruster plume expansion model *Plasma Sources Sci. Technol.* **24** 035006
- [14] Rapp D and Francis W E 1962 Charge exchange between gaseous ions and atoms *J. Chem. Phys.* **37** 2631–45
- [15] Miller J S, Pullins S H, Levandier D J, Chiu Y and Dressler R A 2002 Xenon charge exchange cross sections for electrostatic thruster models *J. Appl. Phys.* **91** 984–91
- [16] Parks D E and Katz I 1979 A preliminary model of ion beam neutralization *14th Int. Electric Propulsion Conf. (Princeton, NJ, October 30–November 1 1979)* (Fairview Park, OH: Electric Rocket Propulsion Society)
- [17] Ashkenazy J and Fruchtmann A 2001 Plasma plume far field analysis *27th Int. Electric Propulsion Conf. (Pasadena, CA, October 15–19 2001)* (Fairview Park, OH: Electric Rocket Propulsion Society)
- [18] Korsun A G and Tverdokhlebova E M 1997 The characteristics of the EP exhaust plume in space *33rd Joint Propulsion Conf. and Exhibit (Seattle, WA, July 6–9 1997)* (Reston, VA: AIAA)
- [19] Dannemayer K, Mazouffre S, Ahedo E and Merino M 2012 Hall effect thruster plasma plume characterization with probe measurements and self-similar fluid models *48th Joint*

- Propulsion Conf. and Exhibit (Atlanta, GA, July 30–August 1 2012)* (Reston, VA: AIAA)
- [20] Cichocki F, Merino M, Ahedo E, Hu Y and Wang J 2015 Fluid versus PIC modeling of a plasma plume expansion *34th Int. Electric Propulsion Conf. (Hyogo-Kobe, Japan, July 6–10 2015)* (Fairview Park, OH: Electric Rocket Propulsion Society)
- [21] Ortega A L, Katz I, Mikellides I G and Goebel D M 2015 Self-consistent model of a high-power Hall thruster plume *IEEE Trans. Plasma Sci.* **43** 2875–86
- [22] Martínez-Sánchez M, Navarro-Cavallé J and Ahedo E 2015 Electron cooling and finite potential drop in a magnetized plasma expansion *Phys. Plasmas* **22** 053501
- [23] Hu Y and Wang J 2014 Fully kinetic simulations of collisionless, mesothermal plasma expansion *13th Spacecraft Charging Technology Conf. (Pasadena, CA, 23–27 June 2014)*
- [24] Wang J, Han D and Hu Y 2015 Kinetic simulations of plasma plume potential in a vacuum chamber *IEEE Trans. Plasma Sci.* **43** 3047–53
- [25] Korsun A G, Tverdokhlebova E M and Gabdullin F F 2004 Mathematical model of hypersonic plasma flows expanding in vacuum *Comput. Phys. Commun.* **164** 434–41
- [26] Oh D Y, Hasting D E, Marrese C M, Haas J M and Gallimore A D 1999 Modeling of SPT-100 thruster plumes and implications for satellite design *J. Propulsion Power* **15** 345–57
- [27] Forest J, Eliasson L and Hilgers A 2001 A new spacecraft plasma simulation software PicUp3D/SPI3 *7th Spacecraft Charging Technology Conf.* vol 476, p 515
- [28] Masselin M 2012 Development of a hybrid PIC code for the simulation of plasma spacecraft interactions *Master's Thesis* University of Stockholm, Sweden
- [29] Wartelski M, Theroude C, Ardura C and Gengembre E 2013 Self-consistent simulations of interactions between spacecraft and plumes of electric thrusters *33rd Int. Electric Propulsion Conf. (Washington, DC, October 7–10 2013)* (Fairview Park, OH: Electric Rocket Propulsion Society)
- [30] Garrigues L, Bareilles J, Boeuf J P and Boyd I D 2002 Modeling of the plasma jet of a stationary plasma thruster *J. Appl. Phys.* **91** 9521–8
- [31] Celik M, Santi M, Cheng S, Martínez-Sánchez M and Peraire J 2003 Hybrid-PIC simulation of a Hall thruster plume on an unstructured grid with DSMC collisions *28th Int. Electric Propulsion Conf. (Toulouse, France, March 17–21 2003)* (Fairview Park, OH: Electric Rocket Propulsion Society)
- [32] Cheng S, Santi M, Celik M, Martínez-Sánchez M and Peraire J 2004 Hybrid PIC-DSMC simulation of a Hall thruster plume on unstructured grids *Comput. Phys. Commun.* **164** 73–9
- [33] Brieda L, Pierru J, Kafafy R and Wang J 2004 Development of the DRACO code for modeling electric propulsion plume interactions *40th Joint Propulsion Conf. and Exhibit* (Reston, VA: AIAA)
- [34] Taccogna F, Pagano D, Scortecci F and Garulli A 2014 Three-dimensional plume simulation of multi-channel thruster configuration *Plasma Sources Sci. Technol.* **23** 065034
- [35] Korkut B and Levin D A 2014 Three dimensional DSMC-PIC simulations of ion thruster plumes with SUGAR *50th Joint Propulsion Conf. (Cleveland, OH, July 28–30 2014)* (Reston, VA: AIAA)
- [36] Korkut B, Li Z and Levin D A 2015 3-D simulation of ion thruster plumes using octree adaptive mesh refinement *IEEE Trans. Plasma Sci.* **43** 1706–21
- [37] Kalentev O, Matyash K, Duras J, Luskow K F, Schneider R, Koch N and Schirra M 2014 Electrostatic ion thrusters-towards predictive modeling *Contrib. Plasma Phys.* **54** 235–48
- [38] Kahnfeld D L 2015 Hybrid plume modeling *Master's Thesis* Mathematisch-Naturwissenschaftliche Fakultät Ernst-Moritz-Arndt-Universität Greifswald, Greifswald, Germany
- [39] Cai C 2015 Numerical studies on plasma plume flows from a cluster of electric propulsion devices *Aerosp. Sci. Technol.* **41** 134–43
- [40] Araki S J, Martin R S, Bilyeu D and Koo J W 2016 SM/MURF: current capabilities and verification as a replacement of AFRL plume simulation tool COLISEUM *52nd Joint Propulsion Conf. (Salt Lake City, UT, July 25–27 2016)* (Reston, VA: AIAA)
- [41] Boyd I and Yim J 2004 Hall thruster plume simulation using a detailed hybrid model *40th Joint Propulsion Conf. and Exhibit* (Reston, VA: AIAA)
- [42] Cichocki F, Domínguez A, Merino M and Ahedo E 2016 A 3D hybrid code to study electric thruster plumes *Space Propulsion Conf. (Rome, Italy, May 2–6 2016)* (Paris, France: 3AF)
- [43] Santi M M 2003 Hall thruster plume simulation using a hybrid-PIC algorithm *PhD Thesis* Massachusetts Institute of Technology, Boston, MA
- [44] Parra F I, Ahedo E, Fife J M and Martínez-Sánchez M 2006 A two-dimensional hybrid model of the Hall thruster discharge *J. Appl. Phys.* **100** 023304
- [45] Parra F, Escobar D and Ahedo E 2006 Improvements on particle accuracy in a Hall thruster hybrid code *42th Joint Propulsion Conf. and Exhibit (Sacramento, CA, July 9–12 2006)* (Reston, VA: AIAA)
- [46] Santos R and Ahedo E 2009 Accuracy improvements in a Hall thruster PIC/fluid code *45th Joint Propulsion Conf. and Exhibit (Denver, CO, August 2–5 2009)* (Reston, VA: AIAA)
- [47] Ahedo E, Santos R and Parra F 2010 Fulfillment of the kinetic Bohm criterion in a quasineutral particle-in-cell model *Phys. Plasmas* **17** 073507
- [48] Santos R and Ahedo E 2009 Implementation of the kinetic Bohm condition in a Hall thruster hybrid code *45th Joint Propulsion Conf. (Denver, CO, August 2–5 2009)* (Reston, VA: AIAA)
- [49] Bird G A 1994 *Molecular Gas Dynamics and the Direct Simulation of Gas Flows* (Oxford: Oxford University Press)
- [50] Tskhakaya D, Matyash K, Schneider R and Taccogna F 2007 The particle-in-cell method *Contrib. Plasma Phys.* **47** 563–94
- [51] Hockney R W and Eastwood J W 1988 *Computer Simulation Using Particles* (Boca Raton, FL: CRC Press)
- [52] Birdsall C K and Fuss D 1997 Clouds-in-clouds, clouds-in-cells physics for many-body plasma simulation *J. Comput. Phys.* **135** 141–8
- [53] Nanbu K and Kitatani Y 1995 An ion-neutral species collision model for particle simulation of glow discharge *J. Phys. D: Appl. Phys.* **28** 324
- [54] Azziz Y, Martínez-Sánchez M and Szabo J 2006 Determination of in-orbit plume characteristics from laboratory measurements *42nd Joint Propulsion Conf. and Exhibit (Sacramento, CA, July 9–12 2006)* (Reston, VA: AIAA)
- [55] Azziz Y 2007 Experimental and theoretical characterization of a Hall thruster plume *PhD Thesis* Massachusetts Institute of Technology, Boston, MA
- [56] Mitchner M and Kruger C H Jr 1973 *Partially Ionized Gases* (Hoboken, NJ: Wiley)
- [57] Bell E W, Djurić N and Dunn G H 1993 Electron-impact ionization of In⁺ and Xe⁺ *Phys. Rev. A* **48** 4286
- [58] Harrison E R and Thompson W B 1959 The low pressure plane symmetric discharge *Proc. Phys. Soc.* **74** 145
- [59] Lapenta G 2002 Particle rezoning for multidimensional kinetic particle-in-cell simulations *J. Comput. Phys.* **181** 317–37

- [60] Martin R S and Cambier J L 2016 Octree particle management for DSMC and PIC simulations *J. Comput. Phys.* **327** 943–66
- [61] Navarro-Cavallé J, Martínez-Sánchez M and Ahedo E 2014 Collisionless electron cooling in a magnetic nozzle *50th Joint Propulsion Conf. (Cleveland, OH, July 28–30 2014)* (Reston, VA: AIAA)
- [62] Merino M, Fajardo P and Ahedo E 2016 Collisionless electron cooling in unmagnetized plasma thruster plumes *52nd Joint Propulsion Conf. (Salt Lake City, UT, July 25–27 2016)* (Reston, VA: AIAA)
- [63] Hu Y and Wang J 2015 Electron properties in collisionless mesothermal plasma expansion: fully kinetic simulations *IEEE Trans. Plasma Sci.* **43** 2832–8
- [64] Navarro-Cavallé J, Correyero S and Ahedo E 2015 Collisionless electron cooling on magnetized plasma expansions: advances on modelling *34th Int. Electric Propulsion Conf. (Kobe, Japan, July 6–10 2015)* (Fairview Park, OH: Electric Rocket Propulsion Society)
- [65] Foster J E, Soulas G C and Patterson M J 2000 Plume and discharge plasma measurements of an NSTAR-type ion thruster *36th Joint Propulsion Conf. and Exhibit (Huntsville, AL, July 16–19 2000)* (Reston, VA: AIAA)
- [66] Brieda L, Nakles M R, Garrett D R, Hargus W A J and Spicer R L 2007 Experimental and numerical examination of the BHT-200 Hall thruster plume *30th Int. Electric Propulsion Conf. (Florence, Italy, September 17–20 2007)* (Fairview Park, OH: Electric Rocket Propulsion Society)
- [67] Myers R M and Manzella D H 1993 Stationary plasma thruster plume characteristics *23rd Int. Electric Propulsion Conf. (Seattle, WA, September 13–16 1993)* (Fairview Park, OH: Electric Rocket Propulsion Society)
- [68] Beal B E, Gallimore A, Hargus W A and Haas J M 2004 Plasma properties in the plume of a Hall thruster cluster *J. Propulsion Power* **20** 985–91
- [69] Beal B E, Gallimore A and Hargus W A 2005 Plasma properties downstream of a low-power Hall thruster *Phys. Plasmas* **12** 123503
- [70] Cohen-Zur A, Fruchtman A and Gany A 2008 The effect of pressure on the plume divergence in the Hall thruster *IEEE Trans. Plasma Sci.* **36** 2069–81
- [71] Merino M, Mauriño J and Ahedo E 2017 Direct-Vlasov study of electron cooling mechanisms in paraxial, unmagnetized plasma thruster plumes *35th Int. Electric Propulsion Conf.* (Fairview Park, OH: Electric Rocket Propulsion Society)
- [72] Taccogna F, Schneider R, Longo S and Capitelli M 2008 Kinetic simulations of a plasma thruster *Plasma Sources Sci. Technol.* **17** 024003
- [73] Carlsson J, Khrabrov A, Kaganovich I, Sommerer T and Keating D 2016 Validation and benchmarking of two particle-in-cell codes for a glow discharge *Plasma Sources Sci. Technol.* **26** 014003
- [74] Polk J, Kakuda R, Anderson J, Brophy J, Rawlin V, Patterson M, Sovey J and Hamley J 1999 Validation of the NSTAR ion propulsion system on the Deep Space One mission—overview and initial results *35th Joint Propulsion Conf. and Exhibit (Los Angeles, CA, June 20–24 1999)* (Reston, VA: AIAA)
- [75] Brophy J R 2002 NASA's Deep Space 1 ion engine (plenary) *Rev. Sci. Instrum.* **73** 1071–8
- [76] Foster J E, Williams G J and Patterson M J 2007 Characterization of an ion thruster neutralizer *J. Propulsion Power* **23** 828–35
- [77] Brophy J R, Garner C E and Mikes S C 2009 Dawn ion propulsion system: Initial checkout after launch *J. Propulsion Power* **25** 1189–202
- [78] Snyder J, Goebel D M, Hofer R R, Polk J E, Wallace N C and Simpson H 2012 Performance evaluation of the T6 ion engine *J. Propulsion Power* **28** 371–9
- [79] Roy R I S, Hastings D E and Gastonis N A 1996 Ion-thruster plume modeling for backflow contamination *J. Spacecr. Rockets* **33** 525–34
- [80] Roy R I S, Hastings D E and Gastonis N A 1996 Numerical study of spacecraft contamination and interactions by ion-thruster effluents *J. Spacecr. Rockets* **33** 535–42
- [81] Wang J, Brinza D and Young M 2001 Three-dimensional particle simulation modeling of ion propulsion plasma environment for Deep Space One *J. Spacecr. Rockets* **38** 433–40
- [82] Taccogna F and Dilecce G 2016 Non-equilibrium in low-temperature plasmas *Eur. Phys. J. D* **70** 251
- [83] Goldston R J and Rutherford P H 1995 *Introduction to Plasma Physics* (Boca Raton, FL: CRC Press)
- [84] Bellan P M 2006 *Fundamentals of Plasma Physics* (Cambridge: Cambridge University Press)
- [85] Bittencourt J A 2013 *Fundamentals of Plasma Physics* (Berlin: Springer)
- [86] Hayashi M 2003 Bibliography of electron and photon cross sections with atoms and molecules published in the 20th century *Xenon Technical Report* National Institute for Fusion Science